Swarthmore College
Works

Senior Theses, Projects, and Awards | Student Scholarship

Spring 2020

Development of Electroanalytical Techniques to Quantify Silver Nanoparticle Dissolution, Aggregation, and Release Kinetics

Zachary J. O'Dell , '20

Follow this and additional works at: https://works.swarthmore.edu/theses

 Part of the Chemistry Commons

Recommended Citation

O'Dell, Zachary J. , '20, "Development of Electroanalytical Techniques to Quantify Silver Nanoparticle Dissolution, Aggregation, and Release Kinetics" (2020). *Senior Theses, Projects, and Awards*. 251.
https://works.swarthmore.edu/theses/251

This work is brought to you for free by Swarthmore College Libraries' Works. It has been accepted for inclusion in Senior Theses, Projects, and Awards by an authorized administrator of Works. For more information, please contact myworks@swarthmore.edu.

Development of Electroanalytical Techniques to Quantify Silver Nanoparticle Dissolution, Aggregation, and Release Kinetics

Presented as a Senior Course Thesis in Chemistry

Zachary J. O'Dell
April 10th, 2020
Swarthmore College
Advisor: Kathryn Riley

Table of Contents

List of Common Abbreviations

AAS – atomic absorption spectroscopy
AgNPs – silver nanoparticles
ASV – anodic stripping voltammetry
BSA – bovine serum albumin
CCC – critical coagulation concentration
CE – capillary electrophoresis
DLCA – diffusion limited colloidal aggregation
DLS – dynamic light scattering
DLVO – Derajaguin-Landau-Verwey-Overbeak
ENMs – engineered nanomaterials
FAAS – flame atomic absorption spectroscopy
HPLC – high performance liquid chromatography
ICP-MS – inductively coupled plasma mass spectrometry
ICP-OES- inductively coupled plasma optical emission spectrometry
LSSV – linear sweep stripping voltammetry
PIV – particle impact voltammetry
RLCA – reaction limited colloidal aggregation
SEM – scanning electron microscopy
SSW – simulated sweat
TEM – transmission electron microscopy
TOC – total organic carbon
UME – ultramicroelectrode

List of Figures

List of Tables

Abstract

Recently, the manufacture of engineered nanomaterials has seen an increase worldwide. This is due to the desirable properties of materials at the nanoscale rather than the bulk scale, such as improved optical, electronic and magnetic properties. Silver nanoparticles (AgNPs) are one of the fastest growing nanomaterials to be incorporated into consumer products due to silver's well known antibacterial and antimicrobial properties. AgNP-enhanced products represent the largest proportion of engineered nanomaterial products on the consumer market, despite questions regarding the life cycle of such products. AgNPs can undergo a number of transformations during their life cycle including dissolution, aggregation, and protein corona formation. Moreover, when incorporated into consumer products, silver can be released in a number of ways, all of which depend on how the nanoparticulate silver was originally incorporated into the product. The release of silver species can have impacts on human and environmental health. Thus, the development of affordable, reliable, and efficient methods of detecting AgNP transformations and release mechanisms is required and was the primary goal of this work.

Electrochemical techniques including linear sweep stripping voltammetry (LSSV) and particle impact voltammetry coupled with UV-vis spectroscopy (PIV/UV-vis) were used to measure Ag(I) and AgNPs in solution, respectively. Specifically, LSSV was used to quantify the dissolution kinetics of AgNPs (release of Ag(I)), while PIV/UV-vis was used to quantify aggregation kinetics and determine colloidal parameters like the critical coagulation concentration (CCC). The optimization of each technique and proof of concept experiments are presented and show that both techniques provide rapid, reproducible quantitative data that is well-supported by other studies in the literature. Finally, these two techniques were coupled to quantify the release kinetics of Ag(I) and in-tact AgNPs from AgNP-enabled cotton fabrics, in an effort to gain insight into silver release mechanisms. Preliminary data suggest that the combined LSSV-PIV/UV-vis technique has significant promise for *in situ* quantification and speciation of released silver and provides several advantages over current techniques. Overall, the work presented herein demonstrates the successful development and application of rapid, affordable and quantitative electroanalytical techniques to evaluate AgNP transformations *in situ*.

Chapter 1: Introduction

The number of commercially available consumer products containing silver nanoparticles (AgNPs) continues to grow due to their unique antimicrobial and antibacterial properties. However, the release of Ag from these products and the transformations of AgNPs in the various environments in which they are deposited is poorly characterized and understood. Thus, the development of affordable, reliable, and efficient methods to measure the release of Ag from the growing number of AgNP-containing consumer products is necessary.

Electrochemistry is a versatile and powerful technique that enables both the measurement of Ag(I) released from AgNPs (a process referred to as dissolution) and the measurement of in-tact AgNPs directly in solution. The former can be accomplished using linear sweep stripping voltammetry (LSSV) and the latter using particle impact voltammetry (PIV). In the present work, each of these techniques was first optimized and applied to study the dissolution and aggregation of AgNPs, respectively. Then, the techniques were combined to study the release of Ag(I) and AgNPs from AgNP-impregnated fabrics. By combining these two distinct electrochemical methods to simultaneously quantify the release of Ag(I) and AgNPs, one can begin to gain insight into the release mechanism of Ag species from AgNP-enabled products. Herein, the motivation for the development of these techniques and the present understanding of AgNP transformations, including the release of Ag species from consumer products, are discussed.

1.1 Silver Nanoparticles and Their Properties

Globally, engineered nanomaterials (ENMs) have experienced exponential growth in production over the past few decades.[1] ENMs are defined as a material of which at least one feature is in the nanometer range (1-100 nm). ENMs have a higher surface area: volume ratio compared to the bulk material, giving nanomaterials unique electrical,[2] magnetic,[3] and optical[4] properties among others. Due to these desirable properties, manufacturers have begun to incorporate ENMs into various consumer products in the fields of medicine, textiles, agriculture, and food packaging.[1,5–9] However, the fate of these ENMs is poorly characterized and unpredictable,[10–12] thus the need for research on how these ENMs will behave in biological and environmental systems is greater now than ever before.

AgNPs are a material of great interest due to silver's antibacterial and antimicrobial properties.[13] AgNPs lead the global increase in production of ENMs, as AgNPs are the most widely utilized ENM in consumer products.[14] AgNPs are used in products such as wound dressings, sunscreens, and other cosmetics in order to prevent any infection of an open cut or sore,[5,6,9,15] but also in some textiles and fabrics, specifically athletic clothing, in order to prevent the growth of bacteria with unpleasant odors.[16–18] However, these desired antibacterial and antimicrobial properties are influenced by the transformations that AgNPs can undergo, including dissolution, aggregation, and protein corona formation; encouraging discussion about the toxicity of AgNPs in various environments.[6,19–21] AgNPs do not selectively target "bad" bacteria, but rather kill all bacteria, including "good" bacteria that are often useful in biological and

environmental processes. AgNP transformations can alter this selectivity (and thus the toxicity), which in turn, dictates the fate and transportation of AgNPs in biological and environmental systems. Understanding the transformations of AgNPs is pivotal to understanding the toxicity of AgNPs in complex environments. As a result, the availability of affordable, reliable quantitative methods to study the ever-increasing amount of AgNP-containing consumer products is of equal importance. The development and application of analytical techniques to study AgNP transformations is one of the primary goals of this work.

1.2 Silver Nanoparticle Transformations

AgNPs can undergo a variety of transformations which alter the structure of the nanoparticle and its properties. Some common transformations include dissolution, aggregation, and the formation of a protein corona.[10,13,22–26] In order to stabilize the AgNPs and prevent these transformations from occurring, AgNPs are often coated with a reducing agent, which can stabilize the AgNPs in one of two ways. First, AgNPs can be coated with charged molecules, such as citrate, that will prevent the AgNPs from interacting with each other. This type of coating stabilizes the AgNPs via electrostatic repulsion and is thus know as electrostatic stabilization.[25] The second type of stabilization is known as steric stabilization, in which long, uncharged molecules coat the particle and prevent AgNPs from interacting with each other by increasing the spatial distance between them.[25] A common coating that uses steric stabilization is polyvinylpyrrolidone (PVP). Still, despite the various coatings applied to AgNPs, it is likely that AgNPs will undergo some type of transformation during their lifetime. Thus, it is crucial to

understand the factors that influence each transformation and how each transformation affects the properties of AgNPs.

Dissolution can be described as the transformation in which Ag(I) is released from AgNPs. Dissolution occurs as AgNPs become unstable in solution in the presence of an oxidizing agent, which causes the nanoparticle to partially dissolve and release Ag(I) into the solution or media. AgNPs undergo oxidative dissolution according to:

$$2\,Ag^0 + \frac{1}{2}\,O_{2\,(aq)} + 2\,H^+ \rightleftharpoons 2\,Ag(I)_{(aq)} + H_2O \qquad (1)$$

Dissolution is the greatest factor influencing the toxicity of AgNPs, as it is Ag(I) that gives AgNPs their antibacterial and antimicrobial properties.[1] Factors such as AgNP coating, solution pH, ionic composition, and ionic strength have been shown to affect AgNP dissolution.[22,23,27–32] Additionally, the physical size of the AgNP affects how fast dissolution occurs, with smaller AgNPs dissolving more rapidly and to a greater extent (higher concentration of dissolved Ag(I)) than larger AgNPs.[33]

Aggregation is a transformation in which two or more nanoparticles come together to form a single, larger particle known as an aggregate.[24,25,34] Aggregation is dependent on the interaction of nanoparticles in solution, which is usually prevented by capping agents such as citrate or PVP. Variables such as AgNP coating, surface charge, and solution conditions such as pH, ionic composition, and ionic strength are all known to affect AgNP aggregation.[29,35–38] At large enough sizes, aggregates can precipitate out of solution. The sedimentation of AgNPs due to aggregation can have a significant impact on their transport. For example, if AgNPs enter a river and immediately

aggregate, then it's important to study how AgNP aggregates affect organisms in the riverbed rather than the surface waters.

Derajaguin-Landau-Verwey-Overbeak (DLVO) theory describes electrostatic aggregation kinetics. Usually, electrostatically stabilized nanoparticles have a repulsive barrier (an electric double layer) that enables them to form a stable, monodisperse colloidal suspension. However, by increasing the ionic strength of the supporting solution the electric double layer is compressed, the repulsive barrier is reduced, and the nanoparticles begin to aggregate. DLVO theory models aggregation kinetics in solutions of various ionic strength via two different approaches: diffusion-limited colloidal aggregation (DLCA) and reaction-limited colloidal aggregation (RLCA).[34] In DLCA, as the name implies, the rate of aggregation is limited by diffusion; meaning that the nanoparticles are completely destabilized in solution and the aggregation rate is only dependent on the rate at which the nanoparticles diffuse toward one another. In RLCA, on the other hand, the rate of aggregation is limited by the reaction conditions; meaning the reaction conditions do not completely destabilize the nanoparticles in solution, so the nanoparticles are stable for a period of time before they begin to aggregate. In this regime, the nanoparticle aggregation rate will increase with increasing ionic strength of the solution. The point at which the RLCA and DLCA regimes intersect is known as the critical coagulation concentration (CCC), the concentration of electrolyte which completely destabilizes the nanoparticles in solution.[34]

The formation of a protein corona on the surface of a nanoparticle differs from aggregation and dissolution since it requires an adsorbate, a protein, to be present in the

sample matrix. This could occur in biological systems such as our bodies when using AgNP-containing products or in environments such as waste water treatment plants and river beds.[19,39] Proteins adsorb to the surface of AgNPs according to their affinity for the nanoparticle, which can be driven by factors such as electrostatic and other van der Waals forces. Many proteins can bind to the same AgNP to form a multi-layer protein corona, where the inner layer (the "hard" corona) is composed of tight binding, kinetically slow binding proteins, and the outer layer (the "soft" corona) is characterized by weaker binding, kinetically fast binding proteins.[19,40,41] The protein corona changes the properties, stability, and reactivity of AgNPs and is another important factor in determining their fate and transport.

Finally, although not a true transformation, researchers have become increasingly interested in studying the release mechanisms of Ag(I) and AgNPs from AgNP-impregnated products such as wound-dressings and fabrics.[16–18,42–45] The release of Ag from AgNP-impregnated products is poorly characterized due to extreme variance in release depending on how the AgNP-impregnated products are manufactured.[18,42,43,45,46] AgNPs can be incorporated into fibers in one of three ways: (1) by embedding the silver additives within a synthetic fiber polymer, (2) by incorporating the silver additives into a polymer solution and then coating the surface of the fiber with this solution, or (3) by synthesizing AgNPs directly onto the surface of the fiber.[42] The variance in manufacturing processes leads to a wide variety of Ag release dynamics; however, researchers have narrowed down the release mechanism to two possibilities. The first is the release of individual AgNPs from the fiber, followed quickly by their aggregation once in solution. The second is the release of AgNPs as small aggregates; that is, the

aggregation process occurs on the fiber itself.[42] Still, it is unclear if, how, and when dissolution of AgNPs may occur; does Ag(I) dissolve directly from AgNPs embedded in the fiber or are AgNPs released from the fiber first, followed by dissolution? These questions coupled with the extreme variability in the quantity and rate of Ag species released from different AgNP-impregnated products is one of the primary motivations for developing facile, cheap, and reliable analytical methods to detect both Ag(I) and AgNPs.

1.3 Common Methods for Measuring Ag(I)

The first step towards developing a method that can measure both Ag(I) and AgNPs in solution is finding a technique that can accurately and reliably measure Ag(I) in solution. As silver is a redox active metal, a straightforward technique for detecting Ag(I) is anodic stripping voltammetry (ASV).[47,48] By holding a working electrode at a specified, constant potential, Ag(I) in solution is reduced to Ag^0, which accumulates at the electrode surface. Then, by "stripping" the electrode (sweeping the potential in the anodic direction), the Ag^0 that accumulated at the electrode surface is oxidized back to Ag(I), and a change in current is observed as a function of the applied potential. This change in current is observed as a peak in the resulting voltammogram, which can be integrated and correlated to the concentration of Ag(I) in solution, with a limit of detection in the parts per billion (ppb) range. In this work, linear sweep stripping voltammetry (LSSV) was optimized to measure the dissolution of AgNPs in various media. The term "linear sweep" refers to the voltammetric excitation signal and describes that the anodic sweep was carried out at a fixed rate (fixed potential per unit time).

Atomic absorption spectroscopy (AAS) is another reliable, sensitive method for measuring Ag(I) in solution.[18,43,49] While having similar, if not slightly better detections limits than electrochemical techniques, AAS is 2-3 times more expensive, requires greater sample preparation, and requires longer experimental times. Most samples have to undergo centrifugation and then acid digestion before they can be analyzed using AAS. In comparison, LSSV is cheap, requires minimal sample preparation, and has a very short experimental time. Thus, LSSV is used as our primary analysis technique, while AAS, specifically flame atomic absorption spectroscopy (FAAS), will be used in the future as a complementary technique to support LSSV findings.

1.4 Common Methods for Measuring AgNPs

Measuring AgNPs is a little more nuanced than measuring Ag(I), as one can measure either the size or concentration of AgNPs in solution, and many techniques are capable of measuring both. In order to obtain AgNP size distributions and information about the particle shape, scanning electron microscopy (SEM) and transmission electron microscopy (TEM) are often used.[42,50] SEM and TEM do not output raw size data, but rather images of the AgNPs must be post-processed using software such as Image J. Further, SEM and TEM are very expensive and time consuming, so electron microscopy data is most often used in an auxiliary fashion. Dynamic light scattering (DLS) is another technique that is useful for obtaining AgNP size distributions.[51] DLS is much cheaper than electron microscopy and provides direct and very detailed information about the hydrodynamic diameter of the particle and the polydispersity of the sample. This is extremely helpful in monitoring the aggregation of AgNPs, as one can tell if a sample of

AgNPs are monodisperse, partially aggregated, or fully aggregated. Additionally, DLS instruments are typically equipped to measure the zeta potential of the AgNPs. Changes in the zeta potential of AgNPs could indicate particle aggregation or the formation of a protein corona. In this study, DLS was used as the primary technique to characterize AgNPs, while SEM was used to complement DLS sizing data.

Various techniques are able to quantify the concentration of AgNPs in solution, including AAS,[18,43,49] inductively coupled plasma mass spectrometry (ICP-MS),[45] and inductively coupled plasma optical emission spectroscopy (ICP-OES).[43] Although these techniques are extremely sensitive and reliable, they are very expensive and require extensive sample preparation time, as discussed previously. UV-vis spectroscopy is a cheap alternative to the techniques mentioned above, although significant sensitivity must be sacrificed. As aforementioned, ENMs, including AgNPs, have novel optical properties compared to the bulk material. AgNPs exhibit a size-dependent surface plasmon resonance band between approximately 400-500 nm, where the wavelength of maximum absorbance, λ_{max}, shifts to longer wavelength with increasing particle size.[52] Thus, UV-vis spectroscopy can be used as a powerful tool to study AgNP aggregation, and is a method we optimize in this study.

A recently-established technique that has the capability of measuring both the size and concentration of AgNPs in solution is an electrochemical technique known as particle impact voltammetry (PIV).[53–63] In this technique, the working electrode is held at an oxidizing potential and the current is measured as a function of time (*i*-*t* curve). As AgNPs diffuse to and subsequently collide with the electrode surface, the AgNP is oxidized to Ag(I). The simultaneous oxidation of several thousand silver atoms at the

electrode surface causes a flux in the number of electrons transferred, generating a spike in the current known as a transient. The magnitude of the transient is determined by the number of electrons that are transferred between the colliding AgNP and the electrode surface. By integrating each transient in the *i-t* curve, we can determine the amount of charge transferred, *Q*, during each collision and can relate this to the diameter of the nanoparticle to obtain size distributions using the following series of equations. First, the experimental *i-t* curve is integrated to determine the total amount of charge, *Q*, transferred during a collision:

$$Q = \int i \, dt \tag{2}$$

Then, the number of atoms, *N*, in the nanoparticle can be determined using:

$$N = \frac{Q}{e} \tag{3}$$

where *e* is the elementary charge constant (1.602×10^{-19} C).[55] Finally, the number of atoms can be used to calculate the nanoparticle radius, *r*, of the colliding AgNP according to:

$$r = \sqrt[3]{\frac{3A_r N}{4\pi N_A \rho}} \tag{4}$$

where A_r is the relative mass of Ag (107.87 g/mol), N_A is Avogadro's number, and ρ is the density of Ag (10.49 g/cm^3).[55] Simultaneously, we can determine the concentration of AgNPs in solution by comparing the frequency of the collisions to the frequency of collisions at various known concentrations. In this way, PIV allows determination of both the concentration and size of AgNPs in solution in a single experimental run. PIV is cheap, requires little sample preparation, and has similar limits of detection as previously

mentioned techniques, and so it possesses significant potential as an analytical technique for the analysis of AgNPs.

1.5 Speciation of Ag(I) and AgNPs

The growth of research interest in the speciation of Ag(I) and AgNPs released from AgNP-enabled consumer products has been spurred by the increase in products available on the market. Specifically with regard to textiles, researchers are interested in understanding what forms of silver are being released (Ag(I), AgNPs, Ag_2O, Ag_2S, etc.) into solution, the quantity of each form of silver being released, and the rate at which silver is being released from these products. While the number of AgNP-impregnated fabrics continues to grow, these questions have only begun to be answered, with the only real consensus being that each product releases silver in a unique way depending on how the product was made. Thus, the current challenge is to develop a cheap, reliable method to determine both the concentration of Ag(I) and AgNPs released from such fabrics to expedite the discovery of other solution or material chemistries that may influence the release mechanism.

There are multiple techniques that have been used in an effort to speciate between Ag(I) and AgNPs released from AgNP-impregnated fabrics. However, most fail to do so in real time and may be overestimating the concentration of AgNPs that are released from such fibers. AAS, ICP-MS, and ICP-OES are all techniques that speciate between Ag(I) and AgNPs using mass balance calculations; meaning that these techniques measure the concentration of Ag(I) in solution and total Ag concentration, and calculate the difference between the two values to be the concentration of AgNPs in solution. This is

accomplished by exposing the fabric to a solution for some period of time, after which the concentration of Ag(I) in solution is measured using atomic spectroscopy. Subsequently, the solution and fabric are subjected to acid digestion (so that all Ag is in the aqueous phase) and the total amount of Ag is measured using atomic spectroscopy. However, during acid digestion AgNPs may not be the only form of Ag remaining in solution, Ag_2S, AgCl, and $AgPO_3$ could all exist, meaning that these techniques could be overestimating the concentration of AgNPs released from AgNP-impregnated fabrics since a direct measurement of AgNPs is not made.[44]

More recent work has aimed to address the limitations of techniques based on mass transfer by developing methods to simultaneously determine the amount of Ag(I) and AgNPs released from AgNP-impregnated fabrics. One group of researchers has used high-performance liquid chromatography (HPLC) coupled with ICP-MS to successfully speciate between Ag(I) and AgNPs.[46] Another group has successfully coupled capillary electrophoresis (CE) to ICP-MS in order to speciate between Ag(I) and AgNPs.[64] While these techniques successfully speciate between the two forms of silver, they are very expensive instruments and require significant expertise, such that they may not be broadly accessible to the scientific community. The goal of this work is to design a technique that is cheap enough to be universally accessible while also being able to reliably and quantitatively speciate between Ag(I) and AgNPs released from AgNP-impregnated fabrics.

1.6 Research Aims

In this work, we first aimed to demonstrate the optimization of the electrochemical technique LSSV to measure Ag(I) in solution. We demonstrated this by determining the rate of dissolution, $k_{dissolution}$, of AgNPs in various complex biological media (in the presence of proteins and in simulated sweat solutions). Next, we developed and optimized a technique to measure AgNP aggregation in solution. This technique combines the electrochemical technique PIV with the orthogonal spectroscopic technique UV-vis spectroscopy. As will be demonstrated herein, this PIV/UV-vis technique is a powerful tool to measure AgNP aggregation in solution. We demonstrated the optimization of this technique by calculating the CCCs of AgNPs in the presence of monovalent and divalent cations (Na^+ and Mg^{2+}, respectively). In order to obtain CCC values, collision frequencies obtained from PIV and aggregation rates, $k_{aggregation}$, obtained from UV-vis were evaluated at various salt concentrations. The agreement in CCC values obtained by these orthogonal techniques were not only in excellent with one another, but also with CCC values reported in the literature. Finally, the coupling of LSSV and PIV/UV-vis was explored as a means to speciate Ag(I) and AgNPs released from AgNP-impregnated fibers in real time. Preliminary data show that, in particular, LSSV and PIV can be carried out in tandem to quantify the concentration of Ag(I) and AgNPs released and that these measurements can be performed repeatedly over time to begin to evaluate release kinetics. Herein, we enumerate the optimization, validation, and application of each technique (LSSV, PIV/UV-vis, and LSSV tandem PIV) for *in situ* quantification of AgNP transformations.

Chapter 2: Materials and Methods

2.1 Quantifying AgNP Dissolution Using LSSV

2.1.1 Reagents

Nitric acid solution (70%), NaCl (99.5%), sodium citrate monobasic (99.5%), sodium chloride (99.5%), urea (98%), lactic acid solution (85%), silver standard solution (1000 mg L^{-1} $AgNO_3$ in 0.5 M HNO_3), and bovine serum albumin (BSA) were purchased from Sigma-Aldrich (St. Louis, MO). Citrate-stabilized NanoXact AgNPs with diameters of 10, 20, and 40 nm (20 mg L^{-1} in 2 mM citrate) were purchased from nanoComposix (San Diego, CA) and used as received. All AgNP solutions were handled in the dark to prevent light-mediated transformations (e.g., dissolution or aggregation).

For the dissolution study conducted in the presence of BSA, all analyses with the exception of circular dichroism measurements were carried out in a buffer solution containing 5 mM sodium citrate and 5 mM NaCl (pH = 6.5; herein, "citrate buffer") prepared in Millipore water (18.2 MΩ.cm at 25°C). The pH of the buffer solution was adjusted through dropwise addition of 0.1 and 1 M sodium hydroxide. A stock solution of 100 μM BSA was prepared in Millipore water. From the concentrated protein stock, two dilute working stock solutions (5 and 1000 nM) were prepared in Millipore water. All protein solutions were aliquoted and frozen at -20°C for later use.

For the dissolution study conducted in simulated sweat (SSW), all analyses were carried out in a solution that contained 0.1% (v/v) lactic acid, 0.1% (w/v) urea, and varying concentrations of NaCl: 0.05%, 0.25%, or 0.50% (w/v). The pH of SSW and

control solutions was adjusted to 4.5, 5.0, or 5.5 through drop-wise addition of 1M and 0.1M NaOH.

2.1.2 Linear Sweep Stripping Voltammetry

Voltammetric measurements were recorded using a BASi Epsilon Eclipse potentiostat and C-3 Cell Stand from Bioanalytical Systems, Inc. (West Lafayette, IN), which was controlled by the provided BASi Epsilon-EC Electrochemical Analyzer software. The C-3 Cell Stand was equipped with automated stirring and sparging. All solutions were sparged with $N_2(g)$ for at least 10 min before electrochemical analysis (final dissolved oxygen concentration ≈ 8.0 mg L^{-1}). The reference electrode was a Ag/AgCl electrode, the counter electrode was a platinum wire, and the working electrode was a glassy carbon electrode (~3 mm in diameter). At the beginning of each week, the working electrode was polished successively with 15, 3, and 1 μm diamond polishes, followed by 0.05 μm alumina polish. At the beginning of each day, the working electrode was polished with 0.05 μm alumina polish. The electrode was sonicated in Millipore water for 30 s following each polishing step. Finally, the electrode was cycled 100 times from -0.5 to 0.35 V/s using cyclic voltammetry. After each use, all electrodes were rinsed thoroughly with Millipore water. Then, the working electrode was placed in a solution of 35% nitric acid for 30 s, rinsed thoroughly with Millipore water, and sonicated in Millipore water for 30 s.

Each day, a working stock solution of the silver standard was prepared to a concentration of 10 mg L^{-1} in Millipore water. Then, a 10-point matrix-matched calibration curve was generated by injecting known volumes of the working stock solution of the silver standard into the citrate buffer. Five stripping voltammograms were

recorded at each concentration. Deposition occurred for 30 s at -0.5 V, followed by a linear sweep from -0.5 to 0.35 V at 0.1 V/s. The limit of detection (LOD) for Ag(I)(*aq*) in citrate buffer was ≈ 7 μg L^{-1}. After calibration, fresh citrate buffer was added to a clean electrochemical cell and was sparged with $N_2(g)$ and stirred for 10 min. For experiments which included protein, the appropriate volume of BSA solution was added to the electrochemical cell to reach the desired concentration of 0.5, 1, or 2 nM. The protein and buffer solution was sparged and stirred prior to analysis. Before AgNPs were added to the solution, a stripping voltammogram was recorded as a blank. An aliquot of AgNPs was subsequently added to the solution so that the final concentration of AgNPs was 1.0 mg L^{-1} and the solution was allowed to stir for 30 s. Stripping voltammograms were recorded every 5 min for a total of 4 h to generate a dissolution curve. Dissolution experiments were run in triplicate. Peak integrations and data analysis were performed using OriginPro 2018b (v.9.55). To determine dissolution rate constants, $k_{\text{dissolution}}$, dissolution curves were fit using the following equation:

$$ln\left(1 - \frac{[Ag(I)]_t}{[AgNP]_0}\right) = -k_{dissolution}t \quad (5)$$

where $[Ag(I)]_t$ represents the concentration of dissolved Ag(I) at some point in time, *t,* after dissolution has begun and $[AgNP]_0$ is the initial concentration of nanoparticulate silver added.

2.1.3 Nanoparticle and Protein Characterization

The AgNP size and morphology were evaluated using a JEOL 7500F field-emission scanning electron microscope (JEOL USA Inc.). Samples of the as-received AgNPs were pipetted onto silicon wafers and dried overnight. An accelerating voltage of

20.0 kV and a probe current of 5 μA were used for analysis. Size distributions were determined by analysis of at least 300 particles using ImageJ (National Institutes of Health). All particles were spherical, and size distributions for AgNPs with nominal diameters of 10, 20, and 40 nm were 15 ± 3, 24 ± 5, and 42 ± 4 nm, respectively.

The average hydrodynamic diameter (d_{DLS}) and zeta potential (ζ) of AgNPs in the absence and presence of BSA were measured using a Malvern Zetasizer Nano-ZS DLS instrument (Malvern, PA). All samples were prepared in citrate buffer that was double-filtered using a 0.2 μm nylon syringe filter. To enhance the signal, the concentrations of AgNPs and BSA were increased for DLS analysis to 4.0 mg L^{-1} and 8 nM, respectively. In this way, the ratio of AgNPs to BSA was consistent with the largest concentration of BSA used in LSSV analysis (1.0 mg L^{-1}AgNPs: 2 nM BSA). Samples were incubated in the dark at room temperature for 30 min prior to analysis. The average hydrodynamic size and zeta potentials were determined for 10, 20, and 40 nm AgNPs at BSA concentrations of 0 and 8 nM prepared in disposable polystyrene cuvettes with a 1 cm path length. The hydrodynamic diameter of AgNPs was measured using backscatter mode at 173º following a 120 s temperature equilibration at 25 ºC, after which time, 5 replicate measurements were recorded. The number of sub-runs per measurement was automatically determined by the instrument with constraints of a minimum of 10 and maximum of 100 sub-runs per measurement.

Absorbance spectra of AgNPs were obtained using a Cary UV-vis spectrophotometer (Agilent Technologies, Inc.). All analyses were conducted using a semi-micro quartz cuvette with a 1 cm path length and samples were prepared in citrate buffer. Absorbance spectra were recorded with the relative concentration of AgNPs and

BSA matching those used in LSSV analyses (constant AgNP concentration of 4.0 mg L^{-1} and BSA concentrations of 0, 2, 4, and 8 nM). Samples were incubated in the dark at room temperature for 30 min prior to analysis. Absorbance spectra were recorded from 300 to 800 nm at a scan rate of 300 nm/min.

The alpha helicity of BSA in the absence and presence of 10, 20, and 40 nm AgNPs was measured using an Aviv CD spectrometer (Aviv Biomedical, Inc.). Samples were prepared in a solution containing just 5 mM NaCl because of the absorption of citrate in the far-UV region. The concentration of BSA was increased to 1 μM in order to obtain adequate absorption for analysis. Because the AgNPs were unable to be appropriately concentrated to maintain the [AgNP]:[BSA] ratio used in other analyses, a constant concentration of 1.0 mg L^{-1} AgNPs was used. Samples were prepared in semi-micro quartz cuvettes with a 1 cm path length. Samples were prepared in triplicate and allowed to incubate in the dark at room temperature for 30 min before analysis. To eliminate spectral interference, blanks were recorded in each sample cuvette, which was filled with 5 mM NaCl. For each replicate sample, 7 scans were recorded from 200 to 260 nm at 25 ºC and with a 2 nm bandwidth. Data analysis was performed using OriginPro 2018b (v.9.55) and involved subtraction of blank CD scans and normalization of the spectra at 260 nm to zero. The alpha helicity of BSA was calculated using the following equations:

$$MRE_{208} = \frac{observed\ CD\ signal\ (mdeg)}{C_p nl \times 10} \quad (6)$$

$$\alpha - helix\ \% = \left[\frac{-MRE_{208} - 4{,}000}{33{,}000 - 4{,}000}\right] \times 100 \quad (7)$$

where C_p is the molar concentration of protein, n is the number of amino acids in the protein, l is the path length, MRE_{208} is the mean residue ellipticity at 208 nm, 4,000 is the mean residue ellipticity of the random coil conformation at 208 nm, and 33,000 is the mean residue ellipticity of the pure alpha helix at 208 nm.

2.2 Quantifying AgNP Aggregation Using PIV/UV-vis

2.2.1 Reagents

Nitric acid solution (70%), NaCl (99.5%), $MgCl_2$ (99.0%), and sodium citrate monobasic (99.5%) were purchased from Sigma-Aldrich (St. Louis, MO). Citrate-stabilized BioPure AgNPs with a nominal diameter of 40 nm (1,000 mg L^{-1} in 2 mM citrate) were purchased from nanoComposix (San Diego, CA) and used as-received. All AgNP solutions were handled in the dark to prevent light-mediated transformations (e.g., dissolution or aggregation).

All analyses were carried out in a buffer solution containing 10 mM sodium citrate and the buffer was adjusted to pH 5.0 through dropwise addition of 0.1 and 1 M sodium hydroxide. Stock solutions of NaCl and $MgCl_2$ were prepared to a concentration of 1M. The appropriate volume of the designated salt stock solution was added to the citrate buffer so that the final concentration of NaCl was between 10 and 100 mM and $MgCl_2$ was between 1 and 5 mM. All solutions were prepared in environmental grade water with a reported total organic carbon (TOC) content less than 20 ppb (Fisher Scientific).

2.2.2 Particle Impact Voltammetry

Voltammetric measurements were recorded using a CH Instruments Electrochemical Analyzer and CS-3A Cell Stand from CH Instruments, Inc. (Austin, TX), which was controlled by the provided CHI630E Electrochemical Analyzer software. The CS-3A Cell Stand was equipped with automated stirring and sparging. The reference electrode was a Ag/AgCl electrode, the counter electrode was a platinum wire, and the working electrode was an 11 μm carbon fiber ultramicroelectrode (UME). At the beginning of each week, the working electrode was polished with 15, 3, and 1 μm diamond polishes. At the beginning of each day, the working electrode was polished with 1 μm diamond polish. The electrode was sonicated in Millipore water for 30 s following each polishing step. Finally, the electrode was cycled 100 times from -0.5 V to 0.6 V at 0.3 V/s using cyclic voltammetry. After each use, all electrodes were rinsed thoroughly with Millipore water. Then, the working electrode was placed in a solution of 35% nitric acid for 30 s, rinsed thoroughly with Millipore water, sonicated in Millipore water for 30 s, lightly polished using 1 μm diamond polish, rinsed thoroughly with Millipore water, and sonicated in Millipore water for 30 s.

2.2.3 UV-Vis Spectroscopy

Absorbance spectra and kinetics of AgNPs were obtained using an Ocean Optics Flame UV-vis spectrophotometer (Ocean Optics, Inc.) equipped with a CCD detector. The modular unit was housed inside of the CS-3A Cell Stand (**Figure A1**) and OceanView software (v.1.5.7) was used for instrument control and data collection. The instrument was allowed to warm-up for 15 min prior to each use, followed by zeroing the absorbance using the citrate buffer. All analyses were conducted using a glass cuvette

with a 1 cm path length and a 3D printed cuvette cap that enabled a three-electrode electrochemical cell and a sparge tube to fit inside the UV-vis cuvette (**Figure A2**). In this way, PIV and UV-vis data could be collected simultaneously. Absorbance spectra were collected using a 6 ms integration time, averaging 10 scans, and using a boxcar width of 2 (averaging two neighboring points on the CCD detector). Kinetic data was simultaneously collected by monitoring the absorbance at 410 nm as a function of time. The OceanView strip chart application was used for kinetic data collection with a linear buffer width of 6,000 and a data update rate every 10 scans.

2.2.4 PIV/UV-vis Experiments

Prior to each run, the 10 mM citrate buffer was stirred and purged with $N_2(g)$ for 10 min. Then, a blank *i-t* curve and absorbance spectrum were recorded. Next, the AgNP stock solution was sonicated for 30 s and the appropriate volume was added to the citrate buffer to a final concentration of 5.0 mg L^{-1}. After the addition of AgNPs, another absorbance spectrum was recorded, and the kinetic absorbance scan was initiated. Finally, the desired NaCl (10, 20, 40, 60, 80, or 100 mM) or $MgCl_2$ (1.0, 2.0, 2.5, 3.0, 4.0, or 5.0 mM) concentration was added to the buffer solution. An absorbance spectrum was immediately recorded, and the PIV experiment was initiated by applying a potential of 0.5 V to the working electrode. The *i-t* curve and kinetic absorbance scan were recorded continuously for 5 min and absorbance spectra were recorded every 60 s during that time. Five replicates were obtained at each salt concentration and peak integration and data analysis was performed using OriginPro 2018b (v.9.55). CCC values were determined from both electrochemical and spectroscopic AgNP aggregation data by

applying a linear fit to the RLCA and DLCA regimes, the intersection of which is the CCC value.

2.2.5 Nanoparticle Characterization

The AgNP size and morphology were evaluated using a JEOL 7500F field-emission scanning electron microscope (JEOL USA, Inc.). Samples of the as-received AgNPs were pipetted onto silicon wafers and dried overnight. An accelerating voltage of 20.0 kV and a probe current of 5 μA were used for analysis. Size distributions were determined by analysis of 400 particles using ImageJ (National Institutes of Health). All particles were spherical, and the size distribution was determined to be 41 ± 6 nm.

The average hydrodynamic diameter (d_{DLS}) and zeta potential (ζ) of AgNPs were measured using a Malvern Zetasizer Nano-ZS DLS instrument (Malvern, PA). All samples were prepared in 10 mM citrate buffer that was double-filtered using a 0.2 μm nylon syringe filter. The concentration of AgNPs was 5.0 μg L^{-1}. The average hydrodynamic size and zeta potential were determined for 40 nm AgNPs at NaCl and $MgCl_2$ concentrations corresponding to those used in the PIV/UV-vis study. The hydrodynamic diameter of AgNPs was measured using backscatter mode at 173º following a 120 s temperature equilibration at 25 ºC for 120 s, after which time, 5 replicate measurements were recorded. The number of sub-runs per measurement was automatically determined by the instrument with constraints of a minimum of 10 and maximum of 100 sub-runs per measurement.

2.3 Quantifying Ag Release from Textiles

2.3.1 Reagents

Nitric acid solution (70%), NaCl (99.5%), lactic acid solution (85%), urea, and silver standard solution (1,000 mg L^{-1} $AgNO_3$ in 0.5 M HNO_3) were purchased from Sigma-Aldrich (St. Louis, MO). Citrate-stabilized BioPure AgNPs with a nominal diameter of 40 nm (1,000 mg L^{-1} in 2 mM citrate) were purchased from nanoComposix (San Diego, CA) and used as-received. All AgNP solutions were handled in the dark to prevent light-mediated transformations (e.g., dissolution or aggregation). AgNP-impregnated cotton fabrics were synthesized by Dr. Justin Gorham at the National Institute of Standards and Technology.[65] Briefly, the fabrics were washed in DI water and heated to a boil. Silver nitrate solution, citrate solution, and sodium borohydride solutions were then added. After 30 minutes, the fabric was allowed to cool before being washed, air dried, and characterized. AgNP fabrics were stored in the dark in a vacuum desiccator to prevent light- or oxygen-mediated transformations.

All analyses were carried out in a simulated sweat (SSW) buffer solution containing 0.05% NaCl, 0.1% urea, and 0.1% lactic acid (pH = 5.0; herein, SSW) prepared in environmental grade water.[66] The pH of the buffer solution was adjusted through dropwise addition of 0.1 and 1 M sodium hydroxide.

2.3.2 LSSV-PIV/UV-vis Experiments

Each day, a working stock solution of the silver standard was prepared to a concentration of 10 mg L^{-1} in environmental grade water. Then, a 6-point matrix matched calibration curve was generated by injecting known volumes of the working stock

solution of the silver standard into the SSW. Five stripping voltammograms were recorded at each concentration. Deposition occurred for 30 s at -0.5 V, followed by a linear sweep from -0.5 V to 0.8 V at 0.1 V/s. Similarly, a 4-point matrix matched calibration curve was generated for PIV that correlated the number of AgNP collisions observed over a 5 min experiment to the AgNP concentration. For this experiment, the working electrode was held at a potential of 0.8 V for the entirety of the 5 min experiment. Only a single *i-t* curve was recorded at each concentration, however the calibration curve exhibited suitable linearity with a daily R^2 value greater than 0.90. After each calibration, the electrodes were cleaned just as described in the procedures above. Then, a fresh cuvette was prepared with 2.5 mL SSW and ≈ 0.0100 g of AgNP-impregnated fabric (an approximately 8 mm × 8 mm swatch). The SSW solution containing the fabric was immediately subjected to LSSV tandem PIV analysis, which was carried out continuously for 1 h. First, LSSV was carried out by depositing any dissolved Ag(I)(*aq*) for 30 s at -0.5 V, followed by a 5 s quiet time and a linear sweep from -0.5 to 0.8 V at 0.1 V/s. Then, PIV was immediately initiated by applying a potential of 0.8 V for 5 min. Then a reverse linear sweep was immediately performed from 0.8 V to -0.5 V at a rate of 0.1 V/s, and the entire LSSV-PIV/reverse sweep was carried out repeatedly for the duration of the hour.

Chapter 3: Using LSSV to Quantify AgNP Dissolution Kinetics in Simulated Biological Matrices

A depiction for the workflow for measuring AgNP dissolution kinetics using LSSV is presented in **Figure 1**. AgNPs are injected into solution where they undergo oxidative dissolution according to Eqn. 1. Dissolved Ag(I) is reduced at the working electrode during deposition (**Figure 1A**), which is carried out in a stirred solution to facilitate mass transfer to the electrode, thereby improving detection sensitivity. After deposition, the potential at the working electrode is swept in the anodic direction. During this sweep, the Ag^0 deposited at the surface of the electrode is oxidized and stripped from the electrode surface, generating a change in current and a corresponding peak in the voltammogram (**Figure 1B**). The area of the peak is proportional to the amount of Ag(I) in solution and is correlated every day using a matrix-matched calibration curve (**Figure 1C**). The process of deposition and stripping can be repeated over time to generate dissolution curves (**Figure 1D**). These dissolution curves can be fit using a first-order

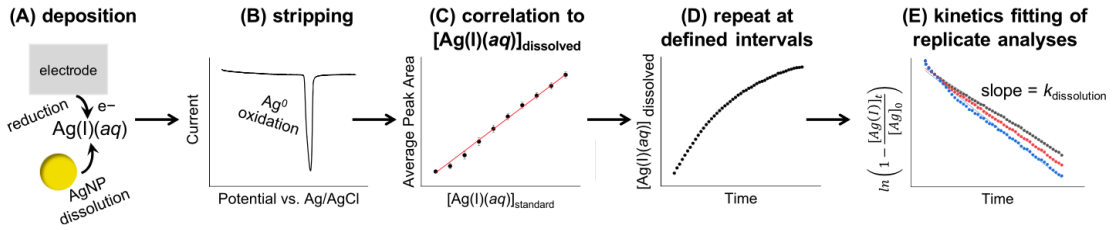

Figure 1. Scheme depicting AgNP dissolution measurement using LSSV. **(A)** Dissolved Ag(I)(*aq*) is reduced (deposited) at the electrode. **(B)** Deposited Ag is oxidized (stripped) during an anodic sweep. **(C)** The area of the stripping peak is correlated to the $[Ag(I)(aq)]_{dissolved}$ using same-day, matrix-matched calibration. **(D)** The measurement is repeated at defined intervals to construct a dissolution curve and **(E)** the dissolution rate constant, $k_{dissolution}$, is determined.

kinetics model to extract dissolution rate constants, $k_{dissolution}$ (**Figure 1E**). Data were fit using Eqn. 5 and the kinetic model fits dissolution experimental data well, with R^2 values better than 0.95.

3.1 Optimization of LSSV

Conditions for the detection of Ag(I) via LSSV were optimized in 5 mM NaCl and 5 mM citrate buffer (pH 6.5). Using a 100 μg L^{-1} solution of Ag(I) standard, the deposition potential, deposition time, and scan rates were optimized. The peak area of the stripping peak increased sequentially as the deposition potential decreased (**Figure 2A,B**); however, the stripping efficiency was reduced at deposition potentials more negative than -0.5 V. Notably, in Figure 2A, the linear sweep does not return to baseline in the range from 0.2-0.4 V, indicating incomplete stripping of silver from the electrode. Thus, the optimized deposition potential used for subsequent analyses was -0.5 V. A marginal increase in peak area was observed with increasing deposition time (**Figure 2C,D**), so a 30 s deposition time was chosen because it provided a slight improvement in the detection sensitivity and reduced the amount of time that the AgNP solution would be perturbed by stirring and application of a potential during deposition. The scan rate had the most significant impact on the magnitude of the peak area, as an increase in scan rate resulted in an increased peak area (**Figure 2E,F**). However, similar to deposition potential, insufficient stripping was observed at sweep rates greater than 0.1 V/s (**Figure 2E**), so a sweep rate of 0.1 V/swas selected for further analysis.

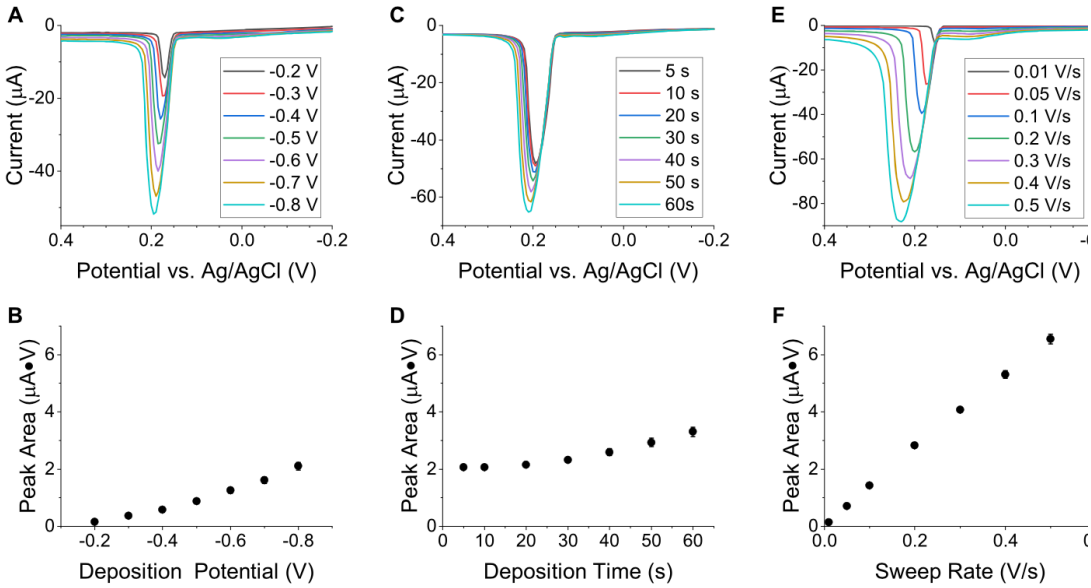

Figure 2. Optimization of LSSV parameters. **(A)** Stripping voltammograms recorded at varying deposition potentials (-0.8 V to -0.2 V), with a constant sweep rate of 0.3 V/s and deposition time of 30 s. **(B)** Corresponding plot of the average area of the stripping peaks as a function of deposition potential. **(C)** Stripping voltammograms recorded at varying deposition times (5 s to 60 s), with a constant deposition potential of -0.5 V and sweep rate of 0.3 V/s. **(D)** Corresponding plot of the average area of the stripping peaks as a function of deposition time. **(E)** Stripping voltammograms recorded at varying sweep rates (0.01 V/s to 0.5 V/s), with a constant deposition potential of -0.5 V and deposition time of 30 s. **(F)** Corresponding plot of the average area of the stripping peaks as a function of sweep rate. All experiments were performed using a 100 μg L^{-1} solution of Ag(I) standard prepared in 5 mM sodium citrate and 5 mM sodium chloride buffer (pH 6.5). All peak areas in B, D, and F represent the average and standard deviation of 5 successive LSSV scans (error bars are too small to be visible in most cases).

3.2 Proof of Concept – Using LSSV to Measure AgNP Dissolution Kinetics in the Presence of BSA

In order to demonstrate that our optimized LSSV technique was capable of measuring Ag(I) dissolved from AgNPs, we obtained dissolution rates of AgNPs in the presence of a model protein, BSA. Before doing so, control experiments were conducted to determine if the presence of BSA would decrease LSSV sensitivity or contribute to electrode fouling, thus preventing the use of LSSV to measure dissolution kinetics. Calibration curves were obtained both in the presence and absence of BSA, and it was shown that the presence of BSA did not deleteriously affect electrode performance or detection sensitivity (**Figure A3**).

With no evidence of electrode biofouling by BSA, AgNP dissolution experiments were pursued. Specifically, AgNP dissolution rate constants, $k_{\text{dissolution}}$, were measured across particle sizes (10, 20, and 40 nm) and BSA concentrations (0-2 nM). As particle size increased, $k_{\text{dissolution}}$ and the total extent of dissolution decreased (**Figure 3**, **Table 1**). For all BSA concentrations evaluated, the dissolution rate for 10 nm AgNPs was statistically different than the dissolution rates of 20 and 40 nm AgNPs. At only the highest concentration of BSA was a statistical difference observed for the dissolution rate of 20 and 40 nm AgNPs. This agrees well with trends found in the literature that smaller AgNPs dissolve at a faster rate and to a greater extent than larger AgNPs.[7,32,67]

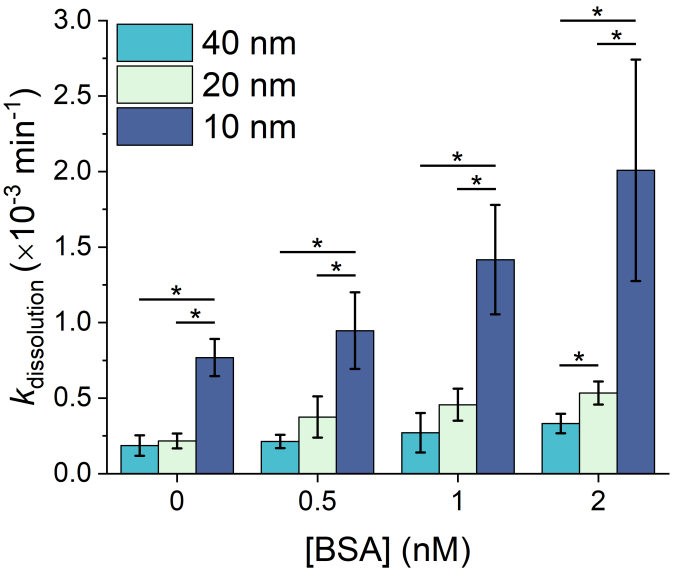

Figure 3. Effect of the [BSA] on the dissolution rate of AgNPs with varying diameter. Each rate constant ($k_{dissolution}$) represents the average and standard deviation of three replicate dissolution measurements using LSSV. All samples were prepared in 5 mM citrate - 5 mM NaCl buffer at pH 6.5. AgNPs were prepared to the same total Ag concentration = 1.0 mg L^{-1} (molar particle concentrations were as follows: 10 nm AgNPs ≈ 290 pM, 20 nm AgNPs ≈ 50 pM, 40 nm AgNPs ≈ 5 pM). Statistical significance was determined using a one-tailed *t*-test evaluated at the 95% (*) confidence interval.

Additionally, dissolution experiments reveal an increase in $k_{dissolution}$ with increasing concentration of BSA across all particle sizes (**Figure 3**). This is consistent with work found in the literature demonstrating protein-driven dissolution of AgNPs, presumably through sequestration of chemisorbed Ag(I) by thiol groups present on BSA.[31,68–70] Upon further evaluation of AgNP dissolution rates, it was found that $k_{dissolution}$ increased linearly as a function of BSA concentration. Interestingly, the magnitude of this increase was observed to be size dependent (**Figure 3**, **Table 1**). Specifically, we observed a 2.1-fold increase in the slope ($dk_{dissolution}$/d[BSA]) for 20 nm AgNPs compared to 40 nm AgNPs, a 3.6-fold increase for 10 nm AgNPs compared to 40 nm AgNPs, and an overall 7.7-fold increase for 10 nm AgNPs compared to 40 nm AgNPs. This suggests a

size-dependent interaction between BSA and the AgNP surface, where BSA mediates more rapid dissolution of smaller AgNPs. To the best of our knowledge, the size-dependent enhancement in AgNP dissolution as a function of protein concentration has not been previously demonstrated. To better understand BSA-enhanced AgNP dissolution, studies were conducted to characterize BSA adsorption on AgNP surfaces.

Table 1. Dependence of AgNP dissolution rates, $k_{dissolution}$, on [BSA] and AgNP diameter[a]

Nominal AgNP Diameter (nm)	Slope	R^2
10	0.59 ± 0.09	0.96
20	0.16 ± 0.03	0.95
40	0.076 ± 0.005	0.99

[a]Experimental conditions are as reported in **Figure 3**. Linear regression slope, standard error in the slope, and correlation coefficients are for the data presented in **Figure 3**.

DLS studies were conducted to monitor changes in the AgNP surface properties upon formation of the BSA-AgNP complex. The average hydrodynamic diameter of 10 and 40 nm AgNPs increased slightly in the presence of BSA, while no change in the hydrodynamic diameter of 20 nm AgNPs was observed (**Figure 4**, **Table A2**). These marginal increases in hydrodynamic diameter are not consistent with the expected increase that would result from monolayer formation of BSA, but they still importantly indicate the colloidal stability of AgNPs in the presence of low concentrations of BSA. Zeta potentials of AgNPs in the absence and presence of BSA were also recorded. A more positive zeta potential was observed for 40 nm AgNPs in the presence of BSA, but no change was observed for 10 and 20 nm AgNPs (**Table A2**). Although increases in the hydrodynamic diameter and zeta potential can be indicative of protein-AgNP complex formation,[69,71,72] the low concentrations of the protein used in this study coupled with

simultaneous dissolution of AgNPs make it difficult to confirm BSA-AgNP complex formation by DLS and zeta potential alone. Thus, UV-vis analyses, specifically Langmuir adsorption isotherms, were also used to evaluate BSA-AgNP complex formation. A marginal increase in the association constant, K_a, was observed with increasing particle size (**Figure A4, Table A3**), which is consistent with data found in the literature.[73–76]

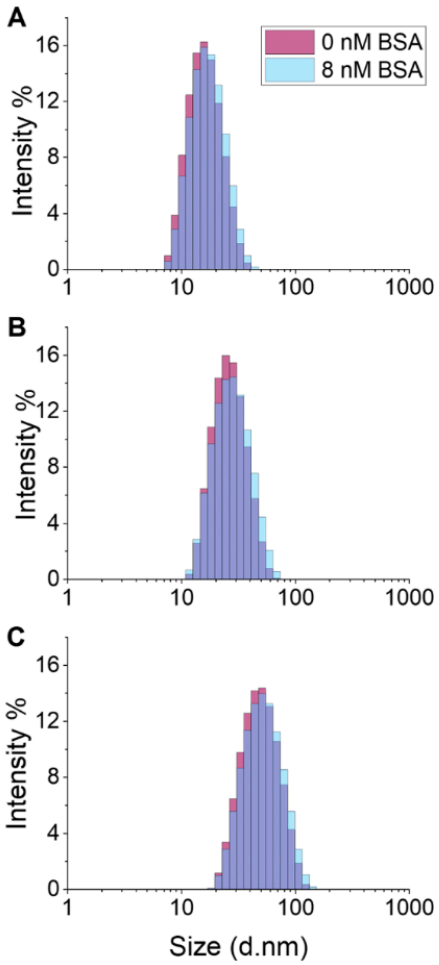

Figure 4. DLS size distributions of **(A)** 10 nm AgNPs, (**B**) 20 nm AgNPs, and (**C**) 40 nm AgNPs with 0 nM BSA (red) and 8 nM BSA (blue). AgNPs were prepared to the same total Ag concentration = 1.0 mg L^{-1} (molar particle concentrations were as follows: 10 nm AgNPs ≈ 290 pM, 20 nm AgNPs ≈ 50 pM, 40 nm AgNPs ≈ 5 pM). All samples were prepared in 5 mM citrate - 5 mM NaCl buffer at pH 6.5.

As a final method to examine the BSA-AgNP interaction, CD was used to measure changes in the % α-helicity of BSA in the presence of AgNPs. The CD spectrum of BSA exhibits two minima in the far-UV region at 208 nm and 222 nm, which are characteristic of α-helical secondary structure.[70,75,77] A decrease in α-helicity of BSA upon interacting with AgNPs can be attributed to loosening of the protein structure.[75,77–79] The largest decrease in α-helicity was observed in the presence of 40 nm AgNPs (7.1% decrease), followed by 10 nm AgNPs (3.4% decrease), and no

significant decrease was observed within error in the presence of 20 nm AgNPs (**Figure 5**, **Table A4**). The subtle difference in % α-helicity between 10 nm and 40 nm AgNPs may be attributed to a difference in curvature, where the flatter surface of 40 nm AgNPs leads to a larger contact surface area and a greater change in protein conformation.[80] As with DLS, zeta potential, and UV-vis experiments, CD data for the 10 nm and 20 nm AgNPs showed a more subtle interaction with BSA. For CD specifically, the concentration of protein is in much greater excess than AgNPs, which may lead to an underestimation of AgNP-induced changes in the % α-helicity of BSA compared to dissolution studies where the proportion of AgNPs was higher.

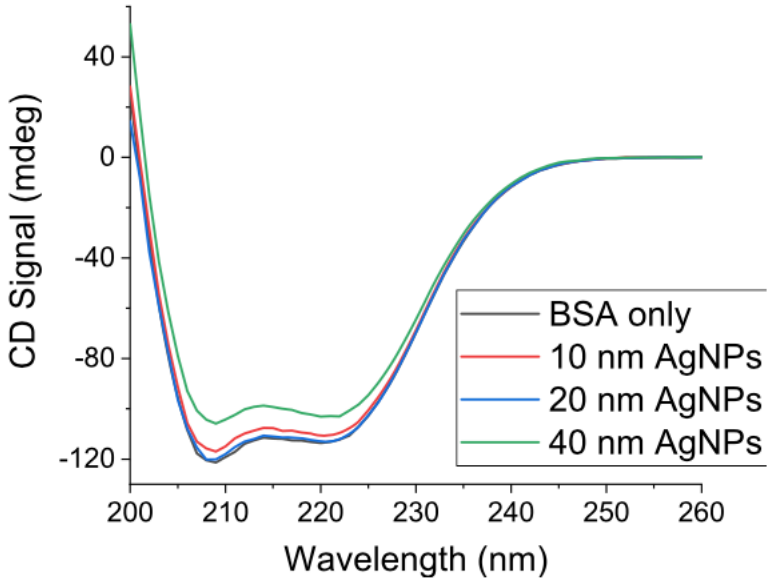

Figure 5. Representative CD spectra demonstrating the effect of AgNPs of varying diameter on the α-helicity of BSA. The concentration of BSA was 1.00 µM. AgNPs were prepared to the same total Ag concentration = 1.00 mg L^{-1} (molar particle concentrations were as follows: 10 nm AgNPs ≈ 290 pM, 20 nm AgNPs ≈ 50 pM, 40 nm AgNPs ≈ 5 pM). All samples were prepared in 5 mM NaCl and incubated for 30 minutes prior to analysis.

Overall, this work suggests that the formation of a BSA-AgNP complex enhances oxidative release of Ag(I) at the surface interface in a AgNP size-dependent manner. This

is consistent with previous work which established smaller AgNPs generally carry greater cytotoxic effects than their larger equivalents,[81] and that these effects have been largely attributed to the increased release of Ag(I) from AgNPs.[1] Overall, in this proof-of-concept experiment, we have established a method to successfully monitor [Ag(I)] in solution using LSSV. We further show that this technique is able to probe AgNP dissolution in the presence of biomolecules, which add to the complexity of dynamic surface chemistries occurring in solution.

3.3 The Effect of SSW Composition on AgNP Dissolution Rates

Due to the use of AgNPs in athletic clothing and working towards the ultimate goal of this work to measure Ag(I) and AgNPs released from fabrics, several LSSV dissolution studies were conducted in SSW solutions to determine the effect of the solution chemistry (pH and NaCl concentration) on AgNP dissolution. The first study held the concentration of SSW components constant (0.05% w/v NaCl, 0.1% v/v lactic acid, and 0.1% w/v urea) and varied the pH (4.5, 5.0, or 5.5) of SSW. It was found that the AgNP dissolution rate decreased with increasing pH (**Figure 6**, **Table A5**). The pH dependence of AgNP dissolution in water and dilute acid solutions is consistent with reports in the literature.[22,29,32,82] This relationship is attributed to the oxidative dissolution of AgNPs (Eqn. 1).[27,29,83] In accordance with Le Châtelier's principle, an increase in pH (decrease in H^+) results in a decrease in Ag(I). Dissolution rate constants determined by LSSV were compared to those found in the literature, and the values were found to agree well with one another (**Table A5**).[33] This suggests that LSSV is able to quantify $k_{\text{dissolution}}$

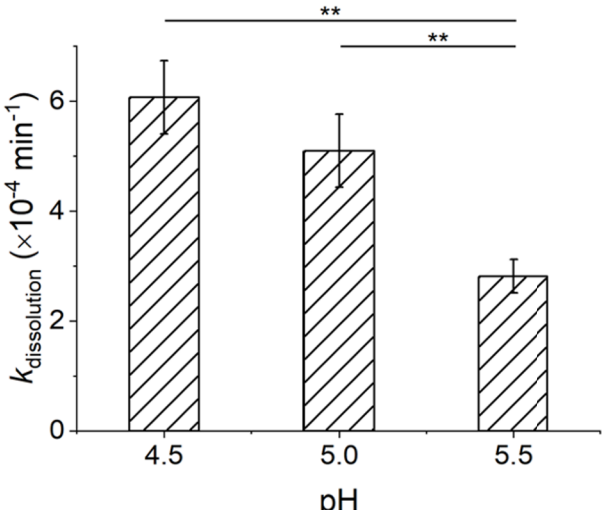

gure 6. Effect of pH on AgNP dissolution rates in SSW solutions. AgNP dissolut rate constants, $k_{dissolution}$, were determined by LSSV. SSW solutions contained 0.05% ıCl (% w/ v), 0.1% lactic acid (% v/v), and 0.1% urea (% w/v) with a pH of 4.5–5 Statistical significance was determined using a two-tailed t-test evaluated at the 99% (**) confidence interval.

in a

differentiate the dissolution rate as a function of pH.

The second LSSV study held the pH of SSW solution constant (pH = 5.0) while varying the concentration of NaCl (0.05%, 0.25%, or 0.50% w/v). It was found that AgNP dissolution rate increased with increasing NaCl concentration (**Figure 7**, **Table A5**), which is consistent with the finding that Cl^- can drive the dissolution of AgNPs through the formation of soluble $AgCl_x^{(x-1)-}$ species.[30,84] With a technique that is able to accurately measure Ag(I) in various media components, we moved on to the development and optimization of PIV/UV-vis, a technique for characterizing and quantifying AgNPs in solution.

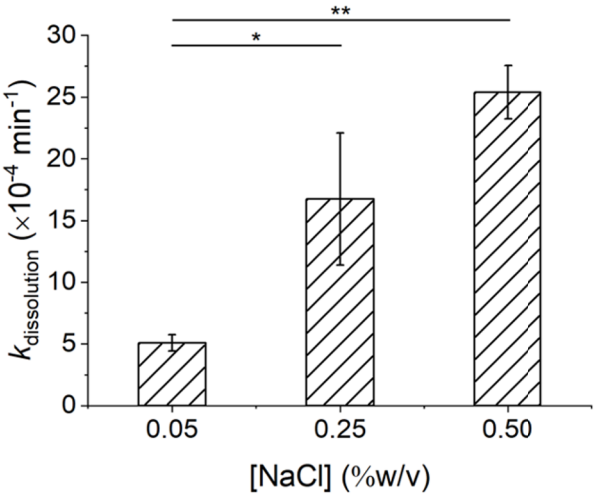

Figure 7. Effect of NaCl concentration on AgNP dissolution rates in SSW solution. AgNP dissolution rate constants, $k_{dissolution}$, were determined by LSSV. SSW solutions ntained 0% to 0.5% NaCl (% w/v), 0.1% lactic acid (% v/v), and 0.1% urea (% w with a constant pH of 5.0. Statistical significance was determined using a two-tailed t-test evaluated at the 95% (*) or 99% (**) confidence intervals.

Chapter 4: Using PIV/UV-vis to Quantify AgNP Aggregation Kinetics

A depiction of the workflow for measuring AgNP aggregation kinetics using PIV/UV-vis is presented in **Figure 8**. AgNPs are injected into solution, where they diffuse to the ultramicroelectrode (UME) surface, which is held at a constant oxidizing potential. When AgNPs collide with the UME they are oxidized and a flux of electrons is transferred at the electrode surface, generating a change in current called a transient (**Figure 8A,B**). Each transient is integrated offline and correlated to the size of the AgNP that collided with the electrode using Eqns. 2-4. The size of AgNPs (d_{AgNP}) is then plotted over time to obtain time resolved AgNP sizing and collision frequency data (**Figure 8C**).

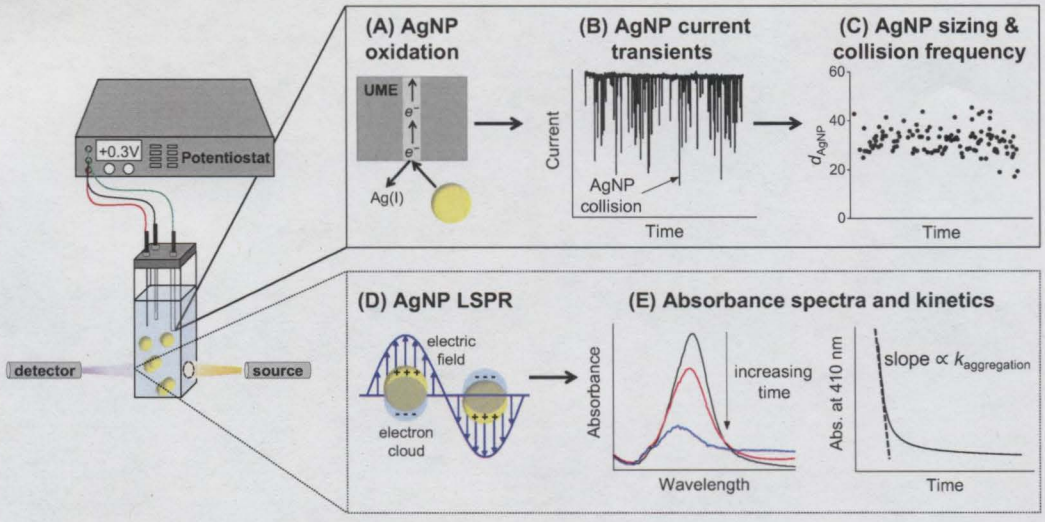

Figure 8. AgNP sizing and determination of aggregation kinetics using PIV/UV-vis. *PIV:* **(A)** AgNPs are oxidized at the ultramicroelectrode generating **(B)** a chronoamperogram, where each current transient represents a single AgNP collision. **(C)** Offline integration of current transients provides AgNP sizes, which can be monitored over time. *UV-vis:* **(D)** The AgNP LSPR enables absorption of electromagnetic radiation in the visible region of the spectrum. **(E)** Changes in the AgNP absorbance spectrum are monitored over time and kinetic absorbance scans are recorded concurrently with PIV chronoamperograms.

Simultaneously, absorbance spectra are recorded every 60 s (**Figure 8E**), and the absorbance at 410 nm is monitored over time, the slope of which is proportional to the aggregation rate, $k_{aggregation}$ (**Figure 8E**).

4.1 Optimization of PIV/UV-vis

Most of the optimization of the PIV/UV-vis technique was completed by my predecessors in the Riley Lab, but I will briefly describe the optimization efforts here. PIV and UV-vis were initially optimized separately, and then combined and optimized by Laela Ezra '19 as part of her thesis. AgNP aggregation is easily measured via UV-vis by monitoring a single wavelength around 410 nm, which corresponds to the λ_{max} of the LSPR band of 40 nm AgNPs. AgNP absorbance is size dependent, as larger AgNPs absorb at larger wavelengths, so significant shifts in the λ_{max} are indicative of AgNP aggregation. Knowing only monomeric 40 nm AgNPs absorb light of wavelength 410 nm, one can effectively monitor both the concentration of monomeric AgNPs in solution and real time aggregation kinetics in the form of a decrease in the absorbance peak at 410 nm as the particles aggregate and their absorbance shifts to a longer wavelength. Ezra worked with various sized AgNPs (10, 20, 40, and 80 nm), finding the optimal λ_{max} to monitor for each size of AgNP, as well as optimizing instrument parameters.[85]

Next, Ezra worked solely with PIV in order to optimize electrochemical parameters, buffer conditions, and the optimal AgNP size for obtaining sufficient signal-to-noise. Previous work in the Riley Lab demonstrates that AgNP aggregation is dependent on the pH of solution as well as NaCl concentration,[86] and Ezra completed a significant amount of optimization to determine the best solution conditions (particularly,

pH and NaCl concentration) to evaluate AgNP aggregation.[85] Ezra also evaluated several AgNP sizes. PIV detection of AgNPs is size-dependent; larger AgNPs diffuse to the UME surface much slower than smaller AgNPs and thus if the particle is too large, no transients will be observed as the large particles cannot migrate to the UME surface fast enough. At the same time, the oxidation of larger AgNPs at the UME surface results in more electrons transferred and greater magnitude current transients leading to improved signal-to-noise. Ultimately, 40 nm AgNPs were chosen as they provided enough transients to quantify collision frequencies (number of current transients per unit time) and sufficient signal-to-noise such that *i-t* curves could be easily integrated to determine AgNP diameters. Electrochemical parameters such as the oxidation potential also had to be optimized for each AgNP size as AgNPs have a distinct "turn on" point above which the AgNPs are oxidized and below which no redox processes occur. For 40 nm particles, Ezra found a turn on potential of approximately 0.15 V, but ultimately used an oxidation potential of 0.5 V to thermodynamically drive the oxidation (**Figure A5**).[85] Finally, Ezra worked to combine and optimize these two techniques into the PIV/UV-vis technique described in **Figure 8** by designing and 3D-printing UV-vis caps allowing for the use of electrochemistry in a UV-vis cuvette, a crucial step towards combining these techniques.

4.2 Proof of Concept – Using PIV/UV-vis to Quantify AgNP Aggregation

In order to test our newly developed PIV/UV-vis technique, we set out to measure AgNP aggregation in the presence of two different salts, NaCl and $MgCl_2$, and to obtain

CCC values. In order to do this, we used 6 different salt concentrations: 3 points at low salt concentration that would fall in the RLCA regime and 3 points at high salt concentration that would fall in the DLCA regime. Examples of data collected at both low and high salt concentrations are provided in **Figure 9**. At low salt concentrations, we observe a significant number of PIV current transients, and almost no decrease in the absorbance measured at 410 nm (**Figure 9A**). Such a small decrease in absorbance is proportional to a very slow aggregation rate, indicating that little to no aggregation occurs on the time scale of this experiment. Thus, it follows in our PIV data, we observe numerous transients throughout the entirety of the experiment, as monomeric AgNPs are able to diffuse to the electrode within the time scale of the experiment. However, at higher salt concentrations, we observe a significant decrease in the number of PIV current

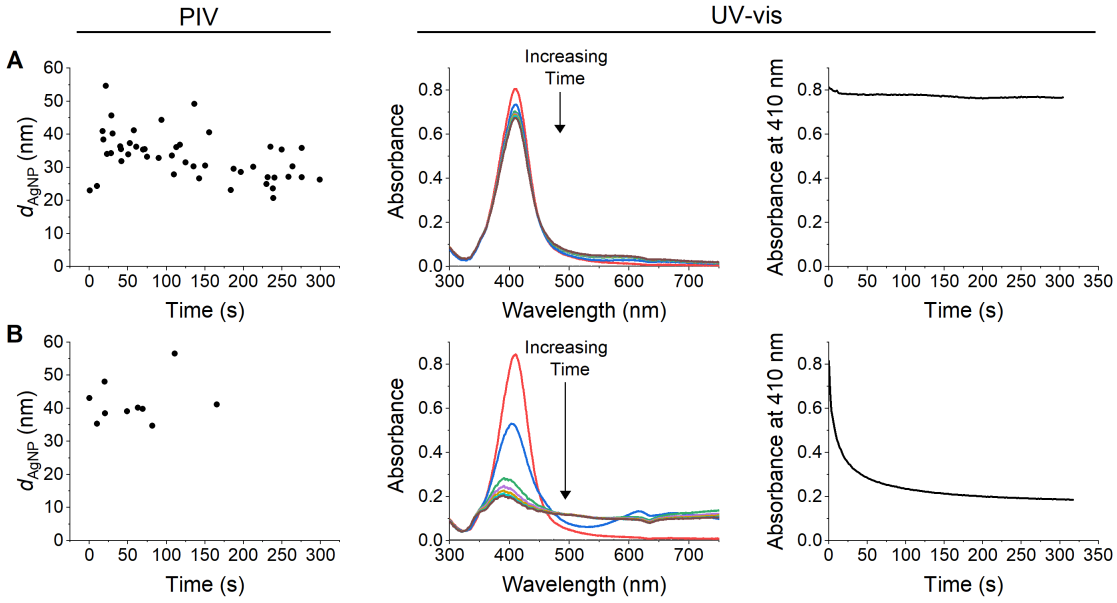

Figure 9. AgNP aggregation measurement using PIV/UV-vis at **(A)** low (20 mM) and **(B)** high (80 mM) salt (NaCl) concentrations. In a single experimental run, AgNP size and collision frequency data can be collected using PIV, while at the same time changes in the UV-vis spectra can be monitored and kinetic absorbance scans can be recorded to obtain AgNP aggregation rates, $k_{aggregation}$.

transients and a much more dramatic decrease in the absorbance measured at 410 nm upon the addition of salt (**Figure 9B**). The large decrease in absorbance is proportional to a very fast aggregation rate, indicating that aggregation rapidly occurs upon the addition of salt. Thus, as AgNPs are rapidly forming larger aggregates, it makes sense that we observe such a small number of transients, especially towards the end of our experiment, as the AgNP aggregates are simply too large to diffuse to the electrode surface on the time scale of our experiment.

We performed 5 replicates of the PIV/UV-vis experiment at each of the 6 concentrations of NaCl. To quantify AgNP collision frequencies, PIV *i-t* curves were integrated, and the number of current transients observed during the duration of the experiment (300 s) was tabulated. Collision frequencies (number of AgNP collisions/s) were averaged at each concentration of NaCl and were normalized to the collision frequency in the DLCA regime (collisions/s_{fast}) according to:

$$normalized\ collision\ frequency = \frac{collisions/s}{collisions/s_{fast}} \tag{8}$$

To quantify the rate of AgNP aggregation, UV-vis kinetic scans were analyzed over the first 30 s according to[23,87,88]:

$$k_{aggregation} = \frac{1}{oN}\frac{dA}{dt} \tag{9}$$

where $k_{aggregation}$ is the aggregation rate constant, (dA/dt) is the slope of the UV-vis kinetic scan measured at 410 nm, N is the initial particle concentration, and o is the optical factor.[88] Then, the attachment efficiencies, α, were calculated according to:

$$\alpha = \frac{k_{slow}}{k_{fast}} \tag{10}$$

where k_{slow} and k_{fast} are the aggregation rate constants in the RLCA and DLCA regimes, respectively.

Finally, the normalized collision frequencies and attachment efficiencies were plotted as function of the NaCl concentration as shown in **Figure 10** (see also **Table A6**). Both plots show a clear transition from the RLCA to the DLCA regime (intersection of the two linear portions of each plot). Looking at the normalized collision frequency data obtained with PIV, we observe at low salt concentrations (below 40 mM), the number of observed transients decreases as the salt concentration increases (**Figure 10A**). This decrease in observed transients is consistent with an increase in the number of aggregated AgNPs in solution that are too large to diffuse to the electrode. This observation is also consistent with the expected behavior of AgNPs in the RLCA regime, whereby colloidal aggregation is limited by the reaction conditions. By adjusting the reaction conditions (adding more NaCl), we can enhance aggregation. However, at high salt concentrations (beyond 40 mM), the number of observed transients more or less remains the same (and relatively infrequent), regardless of further increases in salt concentration (**Figure 10A**). The minimal change in number of transients with increasing salt concentration is indicative of the DLCA regime, whereby colloidal aggregation is only limited by diffusion; the salt concentration no longer influences the rate of aggregation. This is also consistent with the minimal transients observed. In the DLCA regime, the AgNPs are completely destabilized and readily form aggregates that do not diffuse to the UME within the duration of the experiment.

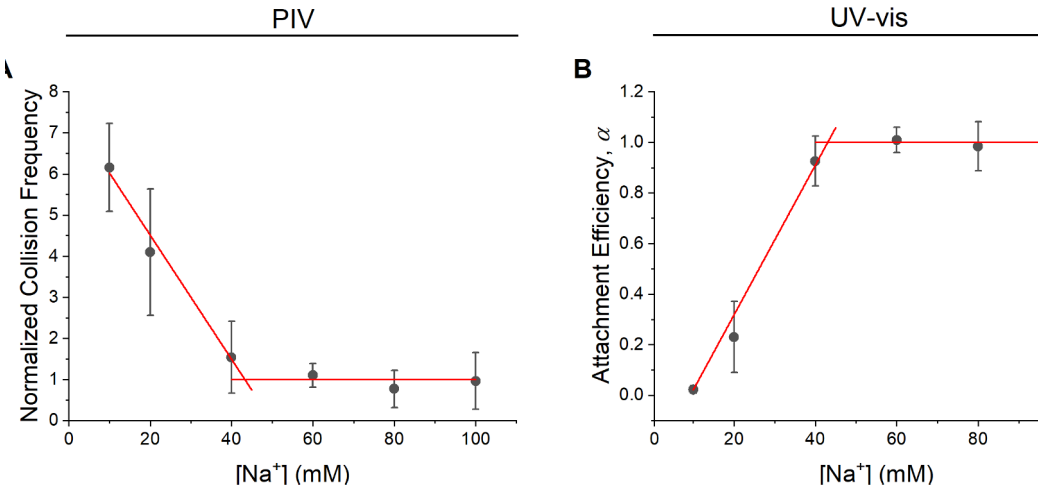

Figure 10. Determination of CCC values of AgNPs in NaCl using PIV/UV-vis. **(A)** Normalized collision frequencies and **(B)** UV-vis attachment efficiencies are plotted as a function of the cation concentration and the intersection of the RLCA and DLCA regimes (linear curves at low and high cation concentration, respectively) is used to termine the CCC.

Looking at the UV-vis or attachment efficiency data, we observe similar trends that at low NaCl concentrations (below 40 mM), AgNP aggregation is dependent upon the concentration, but at high NaCl concentrations (above 40 mM), AgNP aggregation is independent of the concentration (**Figure 10B**). UV-vis normalized data increases as a function of salt concentration because UV-vis measures aggregation rates, which should increase as a function of [NaCl]; whereas PIV normalized data decreases as a function of salt concentration because PIV measures the collision frequency of monomeric AgNPs in solution, which should decrease as a function of [NaCl].

Fitting the RLCA and DLCA regimes in both PIV and UV-vis data allowed us to extract CCC values for AgNPs, which was simply the point of intersection of the two regimes in **Figure 10**. For our PIV experiments, we calculated a CCC value of 43 ± 4 mM Na^+ and for our UV-vis experiments we calculated a CCC value of 43 ± 3 mM Na^+.

Not only do these values agree well with each other, but they also agree well with CCC values reported in the literature (**Table 2**). The accuracy and precision of our PIV/UV-vis technique for AgNPs in NaCl was exceptional, so the validity of the method was confirmed with a divalent cation, Mg^{2+}. As divalent cations have a greater effect on AgNP aggregation than do monovalent cations, smaller concentrations of $MgCl_2$ had to be used, otherwise the experiment was carried out in the same manner as before. Again, the CCC values obtained by PIV/UV-vis analysis were in excellent agreement with one another and with reported values in the literature (**Table 2**; see also **Table A7** and **Figure A6**).

Table 2. CCC values for AgNPs in the presence of monovalent and divalent cations measured by PIV/UV-vis

Cation	CCC (mM)		
	PIV	**UV-vis**	**literature**
Na^+	43 ± 4	43 ± 3	47.6[35], 40[89]
Mg^{2+}	3.0 ± 0.3	3.0 ± 0.1	2.7[35]

Auxiliary DLS experiments were performed to confirm AgNP aggregation. AgNP samples were mixed with each concentration of Na^+ or Mg^{2+} and allowed to incubate for 10 min to allow the aggregates to form prior to analysis. DLS experiments involve significant signal averaging which takes place over the course of approximately 10 min depending on user settings. If measurements had been recorded while the sample was still actively undergoing aggregation, the size distributions obtained would be highly unreliable. DLS measurements confirmed some degree of AgNP aggregation for all

concentrations tested, either from increases in the hydrodynamic diameter and/or the PDI (**Table A8** and **A9**).

Further evaluation of AgNP sizes obtained using the PIV collision data (**Table A8** and **A9**) strengthens the argument that predominately monodisperse AgNPs are generating the observed transients and that AgNP aggregates do not diffuse to the UME during the duration of the experiment. This also supports the data analysis strategy used to determine the CCC using PIV. In a way, monitoring the decrease in PIV collisions with increasing AgNP aggregation (as a proxy for monitoring the decrease in monodisperse AgNPs) is analogous to monitoring the decrease in absorbance at 410 nm as is widely used in UV-vis analysis.

The high precision between PIV and UV-vis analysis may lead to some questions of whether the two analyses being conducted simultaneously have any effect on each other. While one might not question that UV-vis measurement should have no effect on PIV measurement, it may be up for debate as to whether the oxidation of AgNPs at the electrode surface in PIV measurement has any effect on UV-vis measurement. Thus, we set up a control experiment in which we compared our combined PIV/UV-vis analysis with independent PIV and UV-vis analyses. We found that the two methods are truly orthogonal and that aggregation parameters (collision frequencies for PIV and $k_{\text{aggregation}}$ values for UV-vis) are the same whether the methods are performed independently or simultaneously (**Figure A7**, **Table A10**). Thus, UV-vis measurement has no effect on PIV measurement and vice-versa. We conclude that PIV/UV-vis can accurately measure AgNPs aggregation and move on to the development and optimization of an LSSV tandem PIV/UV-vis technique to speciate between Ag(I) and AgNPs in real time.

Chapter 5: Using LSSV-PIV/UV-vis for *In Situ* Speciation of Ag(I) and AgNPs Released from Fabrics

A depiction of the workflow for measuring Ag release using LSSV-PIV/UV-vis is presented in **Figure 11**. At the beginning of each day, same-day matrix-match calibration curves are generated for both Ag(I) and AgNPs. AgNP-impregnated fabrics are then placed into solution and subjected to LSSV (to quantify the concentration of Ag(I) released; **Figure 11A**) followed by PIV (to quantify the concentration and size of AgNPs released; **Figure 11B**). Measurements are repeated over time to evaluate release kinetics.

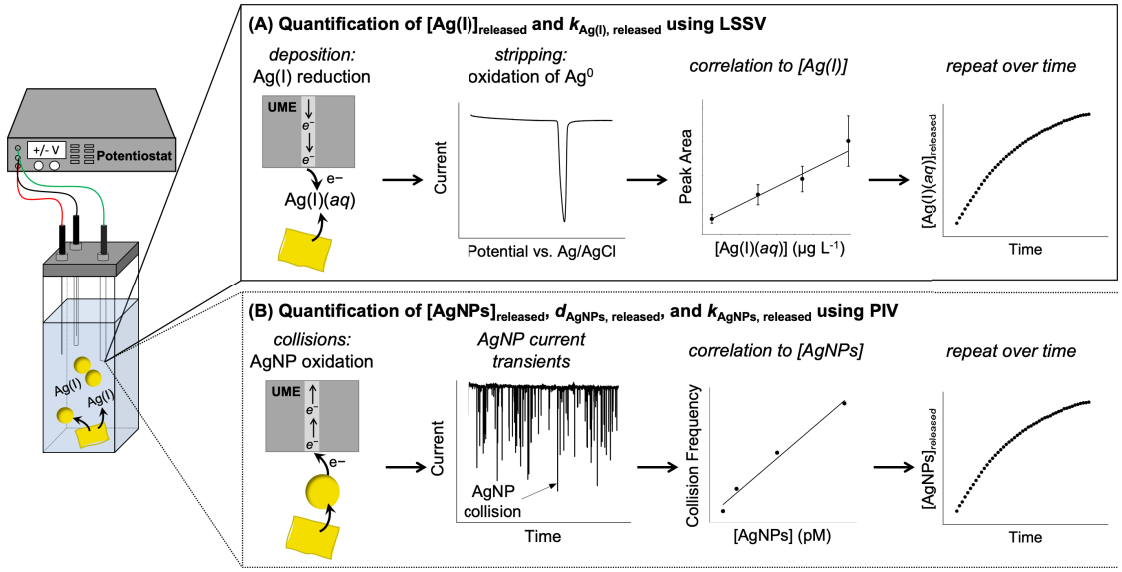

Figure 11. Schematic depicting the measurement of Ag species released from AgNP-impregnated fabrics using LSSV-PIV/UV-vis. **(A)** A swatch of AgNP-impregnated fabric is placed in solution, where it releases Ag(I). The [Ag(I)] released is quantified through deposition and stripping of the dissolved Ag, integration of the peak in the stripping voltammogram, and correlation of the peak are to the [Ag(I)] using a same-day matrix-matched calibration curve. The measurement is repeated over time to evaluate Ag(I) released kinetics. **(B)** Immediately following LSSV, a PIV experiment is conducted to quantify the size and concentration of AgNPs released from the fabric through direct oxidation of the AgNP. The concentration is determined using the collision frequency, which is correlated with a same-day matrix-matched calibration curve and can be measured over time to evaluate release kinetics. The diameter of released AgNPs is determined using Eqns. 2-4.

5.1 Proof of Concept – Using LSSV-PIV/UV-vis to Quantify and Speciate Ag(I) and AgNPs Released from Fabrics

Before full-scale optimization efforts to enable the application of LSSV-PIV/UV-vis to quantify the concentration and rate of Ag species released from AgNP-impregnated fabrics, a simple proof of concept study was performed. Several cotton fabrics were provided by collaborator Justin Gorham at the National Institute of Standards and Technology, including a high load (0.31% Ag loading as determined by X-ray photoelectron spectroscopy, XPS) and low load (0.16% Ag loading, XPS) cotton fabric (**Figure A8**). To provide the best conditions for detecting released Ag species, the high load fabric was chosen for this preliminary study and the fabric was soaked in SSW solution overnight for 22 hours prior to analysis. The next day, matrix-matched calibration curves were constructed for LSSV, PIV, and UV-vis (**Figure 12B**). Then, the SSW solution that the fiber was soaked in was transferred to a PIV/UV-vis cuvette for analysis. LSSV was performed first, followed by PIV, while UV-vis was constantly monitoring the absorbance of the solution throughout the duration of the experiment. The results from this analysis are shown in **Figure 12**.

The presence of both released Ag(I) and AgNPs are detected by LSSV and PIV, respectively, but UV-vis failed to detect any AgNPs in solution (**Figure 12A**). Using LSSV, the [Ag(I)(*aq*)] released was 85 μg L^{-1} (**Figure 12**, left panel) and using PIV, the [AgNPs] released was 5 pM (**Figure 12**, center panel). PIV also enabled us to measure the diameter of the AgNPs that were released from the fabric, which was corroborated by offline DLS analysis ($d_{AgNP,\ PIV} = 50 \pm 9$ nm, $d_{AgNP,\ DLS} = 54 \pm 14$ nm). These values are

also consistent with the diameter of AgNPs on the fabric as determined by SEM (63 ± 13 nm; **Figure A9**). Finally, no absorbance peak was detected in the UV-vis spectrum, which may be due to the concentration of AgNPs released from the fabric being below the LOD of UV-vis, which has much lower sensitivity than PIV. While UV-vis did not have adequate sensitivity to measure AgNPs released from AgNP-impregnated fabrics, PIV and LSSV were sensitive enough to measure released Ag(I) and AgNPs, respectively. Thus, we moved on to the task of optimizing these techniques to quantify the release of Ag in real-time.

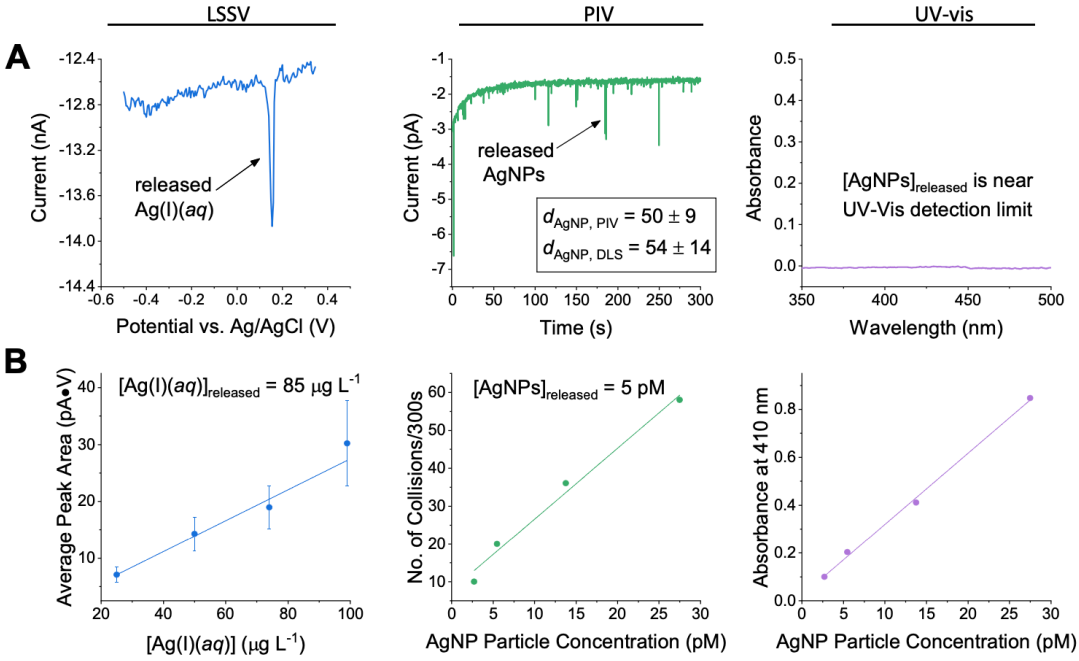

Figure 12. Ag(I)(*aq*) and AgNPs are released from a high-load cotton fabric soaked in SSW. **(A)** Measurement of Ag(I)(aq) and AgNP released from a 1 cm × 1 cm high-load cotton fabric (≈0.0100 g) soaked in 2.5 mL SSW for 22 hours using (from left to right) LSSV, PIV, and UV-vis, respectively. **(B)** Same-day, matrix-matched calibration curves for (from left to right) LSSV, PIV, and UV-vis analyses. The SSW solution contained 0.05% NaCl (w/v), 0.1% lactic acid (v/v), and 0.1% urea (w/v), pH 5.0. LSSV and PIV were conducted with a 10 µm C fiber UME, a Pt wire counter electrode, and a Ag/AgCl reference electrode.

5.2 Optimization of LSSV-PIV/UV-vis

The first piece of optimization was to remove the UV-vis portion of analysis from the technique. UV-vis was simply not sensitive enough to effectively measure the low concentrations of AgNPs released from the fabric, and thus we only used LSSV-PIV to monitor Ag release kinetics moving forward. Next we looked at how we could optimize the LSSV portion of the technique. We noticed in our initial experiments that by increasing electrode deposition time (increasing the amount of time Ag(I) is collected at the electrode surface) we obtain much better signal. Thus, for LSSV-PIV analysis we continued with a 60 s deposition time rather than the 30 s deposition time used in previous LSSV studies. From our initial proof of concept experiment, PIV *i-t* curves did not appear to require any further optimization.

In order to reduce sample preparation steps and create a truly *in situ* technique, we wanted to see if we could measure Ag release from AgNP-impregnated fabrics directly in our sample cuvette rather than having to soak the fabric in SSW solution and then transfer the SSW solution to our sample cuvette. Thus, we placed an approximately 0.0100 g swatch of fabric into 2.5 mL of SSW solution and attempted our LSSV-PIV analysis. The voltammetric signals for both LSSV and PIV were similar to those observed in **Figure 12A**, and we concluded that direct *in situ* measurement of Ag release from AgNP-impregnated fabrics was possible using LSSV-PIV analysis. *In situ* measurements are crucial for measuring Ag release kinetics from fabrics, as it greatly reduces potential error in having to transfer SSW solution to the analysis cuvette. Thus,

all subsequent analyses were carried out with the fabric placed directly in the sample cuvette.

Next, in order to simulate a human exposure scenario, we equipped our LSSV-PIV setup with temperature control. Even after deciding to remove UV-vis from our analysis, we still chose to conduct experiments in the PIV/UV-vis sample cuvette because it had lower sample volume requirements. The Ocean Optics cuvette holder can be easily integrated with a recirculating water bath and so in this way, we could regulate the temperature of the SSW solution at body temperature (37°C) or room temperature (25°C).

Next, a kinetic study was performed both at room temperature and body temperature, where LSSV and PIV analyses were constantly repeated one after another for 1 h. This enables time resolution of approximately 7 min for subsequent determinations of the concentration of Ag(I) and AgNPs. While PIV analysis appeared normal, a dramatic loss of signal was observed in LSSV analysis, even after 1 h of analysis. To diagnose the decreased sensitivity of the LSSV analysis, a control experiment was performed, where a sample of BioPure AgNPs were injected directly into solution and kinetic LSSV-PIV was performed for 1 h. Still, the same results were obtained; AgNPs were detected by PIV, but no Ag(I) was detected by LSSV, even as a known quantity of Ag(I) existed in solution that should have generated significant LSSV signal (**Figure 13A**). Thus, efforts to optimize LSSV were undertaken.

We hypothesized that the lack of signal in our LSSV analysis may be due to the rapid potential switching (from +0.5 V immediately to -0.5 V) that occurred after the conclusion of the PIV portion of the analysis and the start of the next LSSV-PIV

experiment. Thus, we added a third electrochemical step to our analysis; a reverse linear sweep (RLSSV) from 0.5 V to -0.5 V at 0.1 V/s. Using RLSSV between successive LSSV-PIV experiments restored the detection of Ag(I) in the LSSV portion of the analysis (**Figure 13B**).

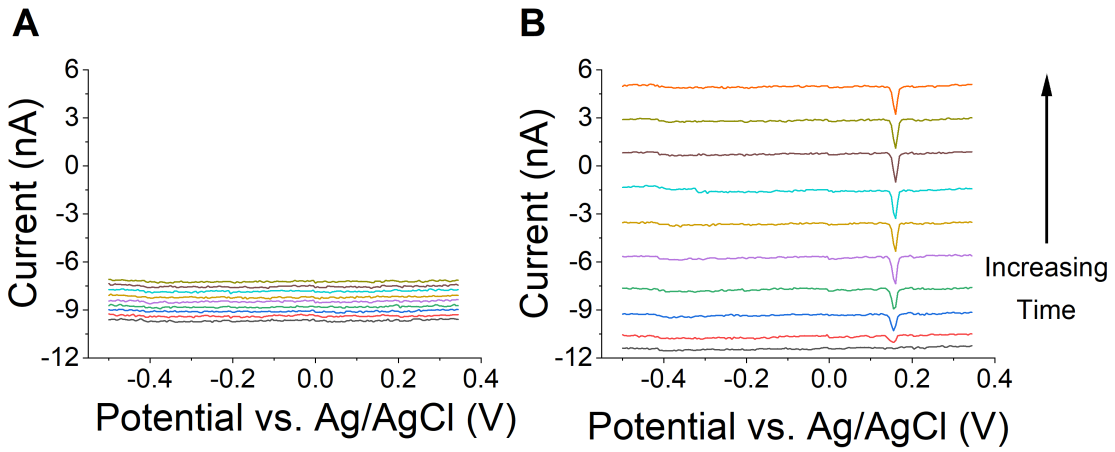

Figure 13. LSSV scans of Ag(I) in the presence of AgNPs **(A)** without a RLSSV step and **(B)** with a RLSSV step. Voltammograms are vertically offset for clarity.

With LSSV signal restored, we again performed a kinetic release study on a AgNP-impregnated fabric. Noticeably more Ag(I) was released at body temperature compared to room temperature (**Figure 14**). However, the PIV signal-to-noise (S/N) ratio became worse with consecutive runs, which made data processing and accurate AgNP characterization almost impossible. Thus, we attempted to optimize the PIV analysis.

In an attempt to increase the S/N and make data processing easier, the oxidation potential used for PIV analysis was increased from 0.5 V to 0.8 V and the data sampling interval was decreased from 0.1 to 0.05 s (more frequent data acquisition). Previous work in our lab has shown that the AgNP redox potential is size-dependent, with larger AgNPs having more anodic oxidation potentials (**Figure A5**), so we hypothesized that increasing

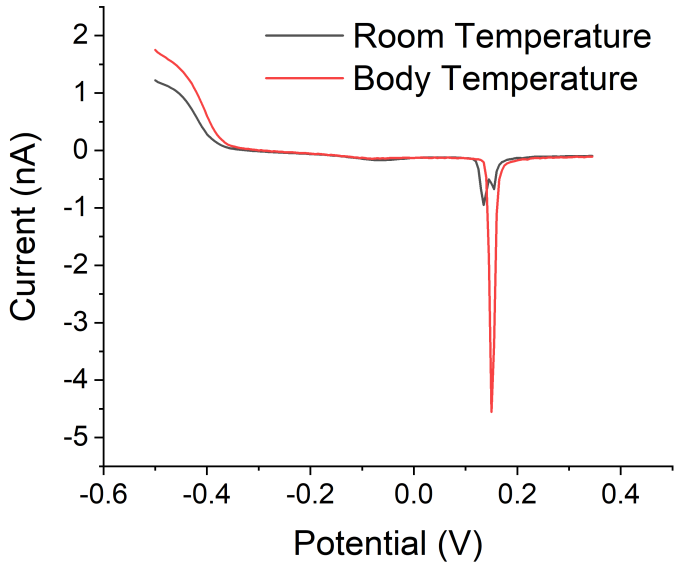

Figure 14. Overlays of LSSV scans of Ag(I) released from a AgNP-impregnated fabric at room temperature and body temperature.

the potential would lead to an increase in the number of transients observed. The AgNPs being released from the fabric had larger diameters than the AgNPs used in our PIV/UV-vis study, and thus we thought an increase in potential would help detect the larger particles. We also hypothesized that decreasing the data sampling interval would enable us to "capture" more transients, which occur on the order of milliseconds, as well as yield sharper peaks that would be easier to integrate. Finally, over the course of these many optimization experiments, it was observed that the PIV background signal was deteriorating over the course of the day but could be somewhat restored by manipulation of the electrode contacts. To eliminate any contribution of the electrode contacts to the PIV measurement, the standard alligator clips were replaced with jacket connectors. The combination of these optimization experiments greatly improved the signal-to-noise ratio and enabled reproducible measurement of AgNP current transients over time (data not shown).

Overall, LSSV-PIV holds significant promise as a rapid, affordable, sensitive, and quantitative method to monitor and speciate Ag released from AgNP-impregnated fabrics. Here, we have demonstrated proof of concept for measuring concentrations of released Ag(I) and AgNPs from fabrics incubated in SSW and have made significant progress in the optimization of the technique to measure release kinetics *in situ*.

Chapter 6: Conclusions and Future Directions

In this work we demonstrate the successful development and optimization of two techniques: LSSV to measure Ag(I) in solution and PIV/UV-vis to measure AgNPs in solution. We move closer to the ultimate goal of combining these two techniques into a single technique capable of not only speciating between Ag(I) and AgNPs released from AgNP-impregnated fabrics, but also measuring their release kinetics. Rigorous optimization was performed on our LSSV-PIV technique that will enable its future application to measure Ag release kinetics from AgNP-impregnated fabrics. Ideally, FAAS, which is a widely accepted technique in the nanotechnology community, will be used to corroborate the findings of LSSV-PIV and validate the technique for measuring Ag release kinetics. Ultimately, LSSV-PIV will be used to study the effect of temperature, pH, and SSW composition on Ag release kinetics from AgNP-impregnated fabrics. The electrochemical techniques developed here have several advantages over more commonly used techniques in the nanotechnology community; (1) they are easily accessible to a wide variety of labs because they are orders of magnitude cheaper ($10,000-$20,000 compared to $200,000+ for commonly used spectroscopy and microscopy techniques); (2) they have better time resolution enabling more reliable kinetic measurements; and (3) they can be performed *in situ*, which greatly reduces sample preparation time and sample loss. In this way, this body of work represents a significant contribution to the nanotechnology community, which is further bolstered by the potential application of these techniques to other redox active metal and metal oxide nanomaterials (e.g., Cu, ZnO) of commercial importance.

Acknowledgments

There are so many people I want to thank for helping me throughout my Swarthmore Chemistry research career. First, I would like to thank all the members of the Riley Lab I was fortunate enough to work with; you all made being in the lab so enjoyable. I have to thank Laela Ezra ’19, Dan Boehmler ’20, Janan Hui ’20, and Chris Chung ’20 specifically for helping and collaborating on work seen throughout this thesis. As already mentioned, Laela developed and optimized almost all of the PIV/UV-vis technique. Janan collected data for the LSSV study in simulated sweat. Chris collected the adsorption isotherms for the LSSV study in the presence of protein. Dan collected almost all of the electrochemistry data for the LSSV study in the presence of protein. So again, thank you and I will miss you all next year!

I would like to thank Ian McGarvey in helping to construct the faraday cage for our LSSV-PIV/UV-vis analysis. The faraday cage as of now includes an electrochemical setup, UV-vis spectrometer, and a water bath. Ian also installed the new jacket connector leads for us. Thanks Ian!

I would like to thank Dr. Justin Gorham at NIST for synthesizing and characterizing AgNP-impregnated fabrics for us; they were exactly what we needed in order to develop and optimize the LSSV-PIV/UV-vis technique.

I would like to thank the Department of Chemistry & Biochemistry and Swarthmore College for granting me the opportunity to conduct research and for funding my research in the Riley Lab for 2 summers. Specifically, thank you to Dr. Chris Graves, Dr. Tom Stephenson, and Dr. Kathryn Riley for serving on my thesis committee and guiding me during the thesis writing process.

Finally, I would like to thank my advisor Dr. Kathryn Riley. You were an amazing mentor throughout my entire 4 years at Swarthmore. I cannot thank you enough for your guidance during research, thesis writing, graduate school applications, and constant jabs at my shooting ability.

References

(1) Calderón-Jiménez, B.; Johnson, M. E.; Montoro Bustos, A. R.; Murphy, K. E.; Winchester, M. R.; Vega Baudrit, J. R. Silver Nanoparticles: Technological Advances, Societal Impacts, and Metrological Challenges. *Frontiers in Chemistry* **2017**, *5*. https://doi.org/10.3389/fchem.2017.00006.

(2) Calahorra, Y.; Shtempluck, O.; Kotchetkov, V.; Yaish, Y. E. Young's Modulus, Residual Stress, and Crystal Orientation of Doubly Clamped Silicon Nanowire Beams. *Nano Lett.* **2015**, *15* (5), 2945–2950. https://doi.org/10.1021/nl5047939.

(3) Reddy, L. H.; Arias, J. L.; Nicolas, J.; Couvreur, P. Magnetic Nanoparticles: Design and Characterization, Toxicity and Biocompatibility, Pharmaceutical and Biomedical Applications. *Chem. Rev.* **2012**, *112* (11), 5818–5878. https://doi.org/10.1021/cr300068p.

(4) Haes, A. J.; Van Duyne, R. P. A Nanoscale Optical Biosensor: Sensitivity and Selectivity of an Approach Based on the Localized Surface Plasmon Resonance Spectroscopy of Triangular Silver Nanoparticles. *J. Am. Chem. Soc.* **2002**, *124* (35), 10596–10604. https://doi.org/10.1021/ja020393x.

(5) Murphy, M.; Ting, K.; Zhang, X.; Soo, C.; Zheng, Z. Current Development of Silver Nanoparticle Preparation, Investigation, and Application in the Field of Medicine. *Journal of Nanomaterials* **2015**, *2015*, 1–12. https://doi.org/10.1155/2015/696918.

(6) Prabhu, S.; Poulose, E. K. Silver Nanoparticles: Mechanism of Antimicrobial Action, Synthesis, Medical Applications, and Toxicity Effects. *International Nano Letters* **2012**, *2* (1). https://doi.org/10.1186/2228-5326-2-32.

(7) Zhang, X.-F.; Liu, Z.-G.; Shen, W.; Gurunathan, S. Silver Nanoparticles: Synthesis, Characterization, Properties, Applications, and Therapeutic Approaches. *IJMS* **2016**, *17* (9), 1534. https://doi.org/10.3390/ijms17091534.

(8) Zhang, F.; Wu, X.; Chen, Y.; Lin, H. Application of Silver Nanoparticles to Cotton Fabric as an Antibacterial Textile Finish. *Fibers Polym* **2009**, *10* (4), 496–501. https://doi.org/10.1007/s12221-009-0496-8.

(9) Konop, M.; Damps, T.; Misicka, A.; Rudnicka, L. Certain Aspects of Silver and Silver Nanoparticles in Wound Care: A Minireview. *Journal of Nanomaterials* **2016**, *2016*, 1–10. https://doi.org/10.1155/2016/7614753.

(10) Furtado, L. M.; Bundschuh, M.; Metcalfe, C. D. Monitoring the Fate and Transformation of Silver Nanoparticles in Natural Waters. *Bulletin of Environmental Contamination and Toxicology* **2016**, *97* (4), 449–455. https://doi.org/10.1007/s00128-016-1888-2.

(11) Pourzahedi, L.; Vance, M.; Eckelman, M. J. Life Cycle Assessment and Release Studies for 15 Nanosilver-Enabled Consumer Products: Investigating Hotspots and

Patterns of Contribution. *Environmental Science & Technology* **2017**, *51* (12), 7148–7158. https://doi.org/10.1021/acs.est.6b05923.

(12) Keller, A. A.; McFerran, S.; Lazareva, A.; Suh, S. Global Life Cycle Releases of Engineered Nanomaterials. *Journal of Nanoparticle Research* **2013**, *15* (6), 1–17.

(13) Le Ouay, B.; Stellacci, F. Antibacterial Activity of Silver Nanoparticles: A Surface Science Insight. *Nano Today* **2015**, *10* (3), 339–354. https://doi.org/10.1016/j.nantod.2015.04.002.

(14) Vance, M. E.; Kuiken, T.; Vejerano, E. P.; McGinnis, S. P.; Hochella, M. F.; Rejeski, D.; Hull, M. S. Nanotechnology in the Real World: Redeveloping the Nanomaterial Consumer Products Inventory. *Beilstein J. Nanotechnol.* **2015**, *6*, 1769–1780. https://doi.org/10.3762/bjnano.6.181.

(15) Sussman, E. M.; Jayanti, P.; Dair, B. J.; Casey, B. J. Assessment of Total Silver and Silver Nanoparticle Extraction from Medical Devices. *Food and Chemical Toxicology* **2015**, *85*, 10–19. https://doi.org/10.1016/j.fct.2015.08.013.

(16) Benn, T. M.; Westerhoff, P. Nanoparticle Silver Released into Water from Commercially Available Sock Fabrics. *Environ. Sci. Technol.* **2008**, *42* (11), 4133–4139. https://doi.org/10.1021/es7032718.

(17) Hedberg, J.; Skoglund, S.; Karlsson, M.-E.; Wold, S.; Odnevall Wallinder, I.; Hedberg, Y. Sequential Studies of Silver Released from Silver Nanoparticles in Aqueous Media Simulating Sweat, Laundry Detergent Solutions and Surface Water. *Environ. Sci. Technol.* **2014**, *48* (13), 7314–7322. https://doi.org/10.1021/es500234y.

(18) Kulthong, K.; Srisung, S.; Boonpavanitchakul, K.; Kangwansupamonkon, W.; Maniratanachote, R. Determination of Silver Nanoparticle Release from Antibacterial Fabrics into Artificial Sweat. **2010**, 9.

(19) Durán, N.; Silveira, C. P.; Durán, M.; Martinez, D. S. T. Silver Nanoparticle Protein Corona and Toxicity: A Mini-Review. *Journal of Nanobiotechnology* **2015**, *13* (1). https://doi.org/10.1186/s12951-015-0114-4.

(20) León-Silva, S.; Fernández-Luqueño, F.; López-Valdez, F. Silver Nanoparticles (AgNP) in the Environment: A Review of Potential Risks on Human and Environmental Health. *Water, Air, & Soil Pollution* **2016**, *227* (9). https://doi.org/10.1007/s11270-016-3022-9.

(21) AshaRani, P. V.; Low Kah Mun, G.; Hande, M. P.; Valiyaveettil, S. Cytotoxicity and Genotoxicity of Silver Nanoparticles in Human Cells. *ACS Nano* **2009**, *3* (2), 279–290. https://doi.org/10.1021/nn800596w.

(22) Elzey, S.; Grassian, V. H. Agglomeration, Isolation and Dissolution of Commercially Manufactured Silver Nanoparticles in Aqueous Environments. *Journal of Nanoparticle Research* **2010**, *12* (5), 1945–1958. https://doi.org/10.1007/s11051-009-9783-y.

(23) Li, X.; Lenhart, J. J. Aggregation and Dissolution of Silver Nanoparticles in Natural Surface Water. *Environmental Science & Technology* **2012**, *46* (10), 5378–5386. https://doi.org/10.1021/es204531y.
(24) Loosli, F.; Omar, F. M.; Carnal, F.; Oriekhova, O.; Clavier, A.; Chai, Z.; Stoll, S. Manufactured Nanoparticle Behavior and Transformations in Aquatic Systems. Importance of Natural Organic Matter. *CHIMIA International Journal for Chemistry* **2014**, *68* (11), 783–787. https://doi.org/10.2533/chimia.2014.783.
(25) Louie, S. M.; Ma, R.; Lowry, G. V. Transformations of Nanomaterials in the Environment. In *Frontiers of Nanoscience*; Elsevier, 2014; Vol. 7, pp 55–87. https://doi.org/10.1016/B978-0-08-099408-6.00002-5.
(26) Levard, C.; Hotze, E. M.; Lowry, G. V.; Brown, G. E. Environmental Transformations of Silver Nanoparticles: Impact on Stability and Toxicity. *Environ. Sci. Technol.* **2012**, *46* (13), 6900–6914. https://doi.org/10.1021/es2037405.
(27) Zhou, W.; Liu, Y.-L.; Stallworth, A. M.; Ye, C.; Lenhart, J. J. Effects of PH, Electrolyte, Humic Acid, and Light Exposure on the Long-Term Fate of Silver Nanoparticles. *Environmental Science & Technology* **2016**, *50* (22), 12214–12224. https://doi.org/10.1021/acs.est.6b03237.
(28) Axson, J. L.; Stark, D. I.; Bondy, A. L.; Capracotta, S. S.; Maynard, A. D.; Philbert, M. A.; Bergin, I. L.; Ault, A. P. Rapid Kinetics of Size and PH-Dependent Dissolution and Aggregation of Silver Nanoparticles in Simulated Gastric Fluid. *J. Phys. Chem. C* **2015**, *119* (35), 20632–20641. https://doi.org/10.1021/acs.jpcc.5b03634.
(29) Fernando, I.; Zhou, Y. Impact of PH on the Stability, Dissolution and Aggregation Kinetics of Silver Nanoparticles. *Chemosphere* **2019**, *216*, 297–305. https://doi.org/10.1016/j.chemosphere.2018.10.122.
(30) Levard, C.; Mitra, S.; Yang, T.; Jew, A. D.; Badireddy, A. R.; Lowry, G. V.; Brown, G. E. Effect of Chloride on the Dissolution Rate of Silver Nanoparticles and Toxicity to *E. Coli*. *Environmental Science & Technology* **2013**, *47* (11), 5738–5745. https://doi.org/10.1021/es400396f.
(31) Liu, C.; Leng, W.; Vikesland, P. J. Controlled Evaluation of the Impacts of Surface Coatings on Silver Nanoparticle Dissolution Rates. *Environmental Science & Technology* **2018**, *52* (5), 2726–2734. https://doi.org/10.1021/acs.est.7b05622.
(32) Peretyazhko, T. S.; Zhang, Q.; Colvin, V. L. Size-Controlled Dissolution of Silver Nanoparticles at Neutral and Acidic PH Conditions: Kinetics and Size Changes. *Environmental Science & Technology* **2014**, *48* (20), 11954–11961. https://doi.org/10.1021/es5023202.

(33) Zhang, W.; Yao, Y.; Sullivan, N.; Chen, Y. Modeling the Primary Size Effects of Citrate-Coated Silver Nanoparticles on Their Ion Release Kinetics. *Environ. Sci. Technol.* **2011**, *45* (10), 4422–4428. https://doi.org/10.1021/es104205a.

(34) Zhang, W. Nanoparticle Aggregation: Principles and Modeling. In *Nanomaterial*; Capco, D. G., Chen, Y., Eds.; Springer Netherlands: Dordrecht, 2014; Vol. 811, pp 19–43. https://doi.org/10.1007/978-94-017-8739-0_2.

(35) Huynh, K. A.; Chen, K. L. Aggregation Kinetics of Citrate and Polyvinylpyrrolidone Coated Silver Nanoparticles in Monovalent and Divalent Electrolyte Solutions. *Environmental Science & Technology* **2011**, *45* (13), 5564–5571. https://doi.org/10.1021/es200157h.

(36) Lodeiro, P.; Achterberg, E. P.; Rey-Castro, C.; El-Shahawi, M. S. Effect of Polymer Coating Composition on the Aggregation Rates of Ag Nanoparticles in NaCl Solutions and Seawaters. *Science of The Total Environment* **2018**, *631–632*, 1153–1162. https://doi.org/10.1016/j.scitotenv.2018.03.131.

(37) Alqadi, M. K.; Abo Noqtah, O. A.; Alzoubi, F. Y.; Alzouby, J.; Aljarrah, K. PH Effect on the Aggregation of Silver Nanoparticles Synthesized by Chemical Reduction. *Mater Sci-Pol* **2014**, *32* (1), 107–111. https://doi.org/10.2478/s13536-013-0166-9.

(38) Badawy, A. M. E.; Luxton, T. P.; Silva, R. G.; Scheckel, K. G.; Suidan, M. T.; Tolaymat, T. M. Impact of Environmental Conditions (PH, Ionic Strength, and Electrolyte Type) on the Surface Charge and Aggregation of Silver Nanoparticles Suspensions. *Environ. Sci. Technol.* **2010**, *44* (4), 1260–1266. https://doi.org/10.1021/es902240k.

(39) Pino, P. del; Pelaz, B.; Zhang, Q.; Maffre, P.; Nienhaus, G. U.; Parak, W. J. Protein Corona Formation around Nanoparticles – from the Past to the Future. *Mater. Horiz.* **2014**, *1* (3), 301–313. https://doi.org/10.1039/C3MH00106G.

(40) Wang, Q.; Lim, M.; Liu, X.; Wang, Z.; Chen, K. L. Influence of Solution Chemistry and Soft Protein Coronas on the Interactions of Silver Nanoparticles with Model Biological Membranes. *Environmental Science & Technology* **2016**, *50* (5), 2301–2309. https://doi.org/10.1021/acs.est.5b04694.

(41) Treuel, L.; Malissek, M. Interactions of Nanoparticles with Proteins: Determination of Equilibrium Constants. In *Cellular and Subcellular Nanotechnology: Methods and Protocols*; Weissig, V., Elbayoumi, T., Olsen, M., Eds.; Humana Press: Totowa, NJ, 2013; pp 225–235.

(42) Holbrook, R. D.; Rykaczewski, K.; Staymates, M. E. Dynamics of Silver Nanoparticle Release from Wound Dressings Revealed via in Situ Nanoscale Imaging. *Journal of Materials Science: Materials in Medicine* **2014**, *25* (11), 2481–2489. https://doi.org/10.1007/s10856-014-5265-6.

(43) Köser, J.; Engelke, M.; Hoppe, M.; Nogowski, A.; Filser, J.; Thöming, J. Predictability of Silver Nanoparticle Speciation and Toxicity in Ecotoxicological Media. *Environ. Sci.: Nano* **2017**, *4* (7), 1470–1483. https://doi.org/10.1039/C7EN00026J.

(44) Lombi, E.; Donner, E.; Scheckel, K. G.; Sekine, R.; Lorenz, C.; Goetz, N. V.; Nowack, B. Silver Speciation and Release in Commercial Antimicrobial Textiles as Influenced by Washing. *Chemosphere* **2014**, *111*, 352–358. https://doi.org/10.1016/j.chemosphere.2014.03.116.

(45) Quadros, M. E.; Pierson, R.; Tulve, N. S.; Willis, R.; Rogers, K.; Thomas, T. A.; Marr, L. C. Release of Silver from Nanotechnology-Based Consumer Products for Children. *Environmental Science & Technology* **2013**, *47* (15), 8894–8901. https://doi.org/10.1021/es4015844.

(46) Soto-Alvaredo, J.; Montes-Bayón, M.; Bettmer, J. Speciation of Silver Nanoparticles and Silver(I) by Reversed-Phase Liquid Chromatography Coupled to ICPMS. *Analytical Chemistry* **2013**, *85* (3), 1316–1321. https://doi.org/10.1021/ac302851d.

(47) Bard, A. J.; Faulkner, L. R. *Electrochemical Methods: Fundamentals and Applications*, Second Edition.; John Wiley & Sons, Inc., 2001.

(48) Compton, R. G.; Banks, C. E. *Understanding Voltammetry*, Third Edition.; World Scientific Publishing Europe Ltd., 2018.

(49) Pasricha, A.; Jangra, S. L.; Singh, N.; Dilbaghi, N.; Sood, K. N.; Arora, K.; Pasricha, R. Comparative Study of Leaching of Silver Nanoparticles from Fabric and Effective Effluent Treatment. *Journal of Environmental Sciences* **2012**, *24* (5), 852–859. https://doi.org/10.1016/S1001-0742(11)60849-8.

(50) Rice, S. B.; Chan, C.; Brown, S. C.; Eschbach, P.; Han, L.; Ensor, D. S.; Stefaniak, A. B.; Bonevich, J.; Vladár, A. E.; Walker, A. R. H.; Zheng, J.; Starnes, C.; Stromberg, A.; Ye, J.; Grulke, E. A. Particle Size Distributions by Transmission Electron Microscopy: An Interlaboratory Comparison Case Study. *Metrologia* **2013**, *50* (6), 663–678. https://doi.org/10.1088/0026-1394/50/6/663.

(51) Ramos, A. P. Dynamic Light Scattering Applied to Nanoparticle Characterization. In *Nanocharacterization Techniques*; Elsevier, 2017; pp 99–110. https://doi.org/10.1016/B978-0-323-49778-7.00004-7.

(52) Lodeiro, P.; Achterberg, E. P.; Pampín, J.; Affatati, A.; El-Shahawi, M. S. Silver Nanoparticles Coated with Natural Polysaccharides as Models to Study AgNP Aggregation Kinetics Using UV-Visible Spectrophotometry upon Discharge in Complex Environments. *Science of The Total Environment* **2016**, *539*, 7–16. https://doi.org/10.1016/j.scitotenv.2015.08.115.

(53) Bartlett, T. R.; Sokolov, S. V.; Compton, R. G. Electrochemical Nanoparticle Sizing Via Nano-Impacts: How Large a Nanoparticle Can Be Measured? *ChemistryOpen* **2015**, *4* (5), 600–605. https://doi.org/10.1002/open.201500061.

(54) Cheng, W.; Compton, R. G. Electrochemical Detection of Nanoparticles by 'Nano-Impact' Methods. *TrAC Trends in Analytical Chemistry* **2014**, *58*, 79–89. https://doi.org/10.1016/j.trac.2014.01.008.

(55) Ellison, J.; Tschulik, K.; Stuart, E. J. E.; Jurkschat, K.; Omanović, D.; Uhlemann, M.; Crossley, A.; Compton, R. G. Get More Out of Your Data: A New Approach to Agglomeration and Aggregation Studies Using Nanoparticle Impact Experiments. *ChemistryOpen* **2013**, *2* (2), 69–75. https://doi.org/10.1002/open.201300005.

(56) Kätelhön, E.; Compton, R. G. Understanding Nano-Impacts: Impact Times and near-Wall Hindered Diffusion. *Chem. Sci.* **2014**, *5* (12), 4592–4598. https://doi.org/10.1039/C4SC02288B.

(57) Kätelhön, E.; Feng, A.; Cheng, W.; Eloul, S.; Batchelor-McAuley, C.; Compton, R. G. Understanding Nano-Impact Current Spikes: Electrochemical Doping of Impacting Nanoparticles. *The Journal of Physical Chemistry C* **2016**, *120* (30), 17029–17034. https://doi.org/10.1021/acs.jpcc.6b04289.

(58) Ly, L. S. Y.; Batchelor-McAuley, C.; Tschulik, K.; Kätelhön, E.; Compton, R. G. A Critical Evaluation of the Interpretation of Electrocatalytic Nanoimpacts. *The Journal of Physical Chemistry C* **2014**, *118* (31), 17756–17763. https://doi.org/10.1021/jp504968j.

(59) Mirkin, M. V.; Sun, T.; Yu, Y.; Zhou, M. Electrochemistry at One Nanoparticle. *Accounts of Chemical Research* **2016**, *49* (10), 2328–2335. https://doi.org/10.1021/acs.accounts.6b00294.

(60) Rees, N. V.; Zhou, Y.-G.; Compton, R. G. Making Contact: Charge Transfer during Particle–Electrode Collisions. *RSC Adv.* **2012**, *2* (2), 379–384. https://doi.org/10.1039/C2RA01100J.

(61) Toh, H. S.; Compton, R. G. 'Nano-Impacts': An Electrochemical Technique for Nanoparticle Sizing in Optically Opaque Solutions. *ChemistryOpen* **2015**, *4* (3), 261–263. https://doi.org/10.1002/open.201402161.

(62) Xiao, X.; Fan, F.-R. F.; Zhou, J.; Bard, A. J. Current Transients in Single Nanoparticle Collision Events. *Journal of the American Chemical Society* **2008**, *130* (49), 16669–16677. https://doi.org/10.1021/ja8051393.

(63) Zhou, Y.-G.; Rees, N. V.; Compton, R. G. The Electrochemical Detection and Characterization of Silver Nanoparticles in Aqueous Solution. *Angewandte Chemie International Edition* **2011**, *50* (18), 4219–4221. https://doi.org/10.1002/anie.201100885.

(64) Michalke, B.; Vinković-Vrček, I. Speciation of Nano and Ionic Form of Silver with Capillary Electrophoresis-Inductively Coupled Plasma Mass Spectrometry. *Journal of Chromatography A* **2018**, *1572*, 162–171. https://doi.org/10.1016/j.chroma.2018.08.031.

(65) Gorham, J. M.; Murphy, K.; Liu, J.; Tselenchuk, D.; Stan, G.; Nguyen, T. M.; Holbrook, R. D.; Winchester, M.; Cook, R. F.; MacCuspie, R. I.; Hackley, V. A. *Preparation of Silver Nanoparticle Loaded Cotton Threads to Facilitate Measurement Development for Textile Applications*; NIST SP 1200-8; National Institute of Standards and Technology, 2015; p NIST SP 1200-8. https://doi.org/10.6028/NIST.SP.1200-8.

(66) Marques, M.; Löbenberg, R.; Almukainzi, M. *Simulated Biological Fluids with Possible Application in Dissolution Testing*; 2011; Vol. 18. https://doi.org/10.14227/DT180311P15.

(67) Ma, R.; Levard, C.; Marinakos, S. M.; Cheng, Y.; Liu, J.; Michel, F. M.; Brown, G. E.; Lowry, G. V. Size-Controlled Dissolution of Organic-Coated Silver Nanoparticles. *Environ. Sci. Technol.* **2012**, *46* (2), 752–759. https://doi.org/10.1021/es201686j.

(68) Martinolich, A. J.; Park, G.; Nakamoto, M. Y.; Gate, R. E.; Wheeler, K. E. Structural and Functional Effects of Cu Metalloprotein-Driven Silver Nanoparticle Dissolution. *Environmental Science & Technology* **2012**, *46* (11), 6355–6362. https://doi.org/10.1021/es300901h.

(69) Ostermeyer, A.-K.; Kostigen Mumuper, C.; Semprini, L.; Radniecki, T. Influence of Bovine Serum Albumin and Alginate on Silver Nanoparticle Dissolution and Toxicity to *Nitrosomonas Europaea*. *Environmental Science & Technology* **2013**, *47* (24), 14403–14410. https://doi.org/10.1021/es4033106.

(70) Wang, X.; Herting, G.; Odnevall Wallinder, I.; Blomberg, E. Adsorption of Bovine Serum Albumin on Silver Surfaces Enhances the Release of Silver at PH Neutral Conditions. *Physical Chemistry Chemical Physics* **2015**, *17* (28), 18524–18534. https://doi.org/10.1039/C5CP02306H.

(71) Shannahan, J. H.; Lai, X.; Ke, P. C.; Podila, R.; Brown, J. M.; Witzmann, F. A. Silver Nanoparticle Protein Corona Composition in Cell Culture Media. *PLoS ONE* **2013**, *8* (9), e74001. https://doi.org/10.1371/journal.pone.0074001.

(72) Brown, J.; Shannahan, J.; Podila, R. A Hyperspectral and Toxicological Analysis of Protein Corona Impact on Silver Nanoparticle Properties, Intracellular Modifications, and Macrophage Activation. *International Journal of Nanomedicine* **2015**, 6509. https://doi.org/10.2147/IJN.S92570.

(73) Lacerda, S. H. D. P.; Park, J. J.; Meuse, C.; Pristinski, D.; Becker, M. L.; Karim, A.; Douglas, J. F. Interaction of Gold Nanoparticles with Common Human Blood Proteins. *ACS Nano* **2010**, *4* (1), 365–379. https://doi.org/10.1021/nn9011187.

(74) Brewer, S. H.; Glomm, W. R.; Johnson, M. C.; Knag, M. K.; Franzen, S. Probing BSA Binding to Citrate-Coated Gold Nanoparticles and Surfaces. *Langmuir* **2005**, *21* (20), 9303–9307. https://doi.org/10.1021/la050588t.

(75) Dasgupta, N.; Ranjan, S.; Patra, D.; Srivastava, P.; Kumar, A.; Ramalingam, C. Bovine Serum Albumin Interacts with Silver Nanoparticles with a "Side-on" or "End on" Conformation. *Chemico-Biological Interactions* **2016**, *253*, 100–111. https://doi.org/10.1016/j.cbi.2016.05.018.

(76) Dennison, J. M.; Zupancic, J. M.; Lin, W.; Dwyer, J. H.; Murphy, C. J. Protein Adsorption to Charged Gold Nanospheres as a Function of Protein Deformability. *Langmuir* **2017**, *33* (31), 7751–7761. https://doi.org/10.1021/acs.langmuir.7b01909.

(77) Wang, G.; Lu, Y.; Hou, H.; Liu, Y. Probing the Binding Behavior and Kinetics of Silver Nanoparticles with Bovine Serum Albumin. *RSC Advances* **2017**, *7* (15), 9393–9401. https://doi.org/10.1039/C6RA26089F.

(78) Huang, R.; Carney, R. P.; Ikuma, K.; Stellacci, F.; Lau, B. L. T. Effects of Surface Compositional and Structural Heterogeneity on Nanoparticle–Protein Interactions: Different Protein Configurations. *ACS Nano* **2014**, *8* (6), 5402–5412. https://doi.org/10.1021/nn501203k.

(79) Ban, D. K.; Paul, S. Protein Corona over Silver Nanoparticles Triggers Conformational Change of Proteins and Drop in Bactericidal Potential of Nanoparticles: Polyethylene Glycol Capping as Preventive Strategy. *Colloids and Surfaces B: Biointerfaces* **2016**, *146*, 577–584. https://doi.org/10.1016/j.colsurfb.2016.06.050.

(80) Lundqvist, M.; Sethson, I.; Jonsson, B.-H. Protein Adsorption onto Silica Nanoparticles: Conformational Changes Depend on the Particles' Curvature and the Protein Stability. *Langmuir* **2004**, *20* (24), 10639–10647. https://doi.org/10.1021/la0484725.

(81) Choi, Y.; Kim, H.-A.; Kim, K.-W.; Lee, B.-T. Comparative Toxicity of Silver Nanoparticles and Silver Ions to Escherichia Coli. *Journal of Environmental Sciences* **2018**, *66*, 50–60. https://doi.org/10.1016/j.jes.2017.04.028.

(82) Liu, J.; Hurt, R. H. Ion Release Kinetics and Particle Persistence in Aqueous Nano-Silver Colloids. *Environ. Sci. Technol.* **2010**, *44* (6), 2169–2175. https://doi.org/10.1021/es9035557.

(83) Zook, J. M.; Halter, M. D.; Cleveland, D.; Long, S. E. Disentangling the Effects of Polymer Coatings on Silver Nanoparticle Agglomeration, Dissolution, and Toxicity to Determine Mechanisms of Nanotoxicity. *Journal of Nanoparticle Research* **2012**, *14* (10). https://doi.org/10.1007/s11051-012-1165-1.

(84) Kent, R. D.; Vikesland, P. J. Controlled Evaluation of Silver Nanoparticle Dissolution Using Atomic Force Microscopy. *Environmental Science & Technology* **2012**, *46* (13), 6977–6984. https://doi.org/10.1021/es203475a.
(85) Ezra, L. Monitoring Silver Nanoparticle Aggregation In Situ by Integrating Particle Impact Voltammetry and UV- Vis Spectroscopy. Senior Course Thesis in Chemistry, Swarthmore College, 2019.
(86) Hui, J.; O'Dell, Z. J.; Rao, A.; Riley, K. R. In Situ Quantification of Silver Nanoparticle Dissolution Kinetics in Simulated Sweat Using Linear Sweep Stripping Voltammetry. *Environ. Sci. Technol.* **2019**, acs.est.9b04151. https://doi.org/10.1021/acs.est.9b04151.
(87) Baalousha, M.; Nur, Y.; Römer, I.; Tejamaya, M.; Lead, J. R. Effect of Monovalent and Divalent Cations, Anions and Fulvic Acid on Aggregation of Citrate-Coated Silver Nanoparticles. *Science of The Total Environment* **2013**, *454–455*, 119–131. https://doi.org/10.1016/j.scitotenv.2013.02.093.
(88) Virden, J. W.; Berg, J. C. The Use of Photon Correlation Spectroscopy for Estimating the Rate Constant for Doublet Formation in an Aggregating Colloidal Dispersion. *Journal of colloid and interface science* **1992**, *149* (2), 528–535.
(89) Li, X.; Lenhart, J. J.; Walker, H. W. Aggregation Kinetics and Dissolution of Coated Silver Nanoparticles. *Langmuir* **2012**, *28* (2), 1095–1104. https://doi.org/10.1021/la202328n.

Appendix

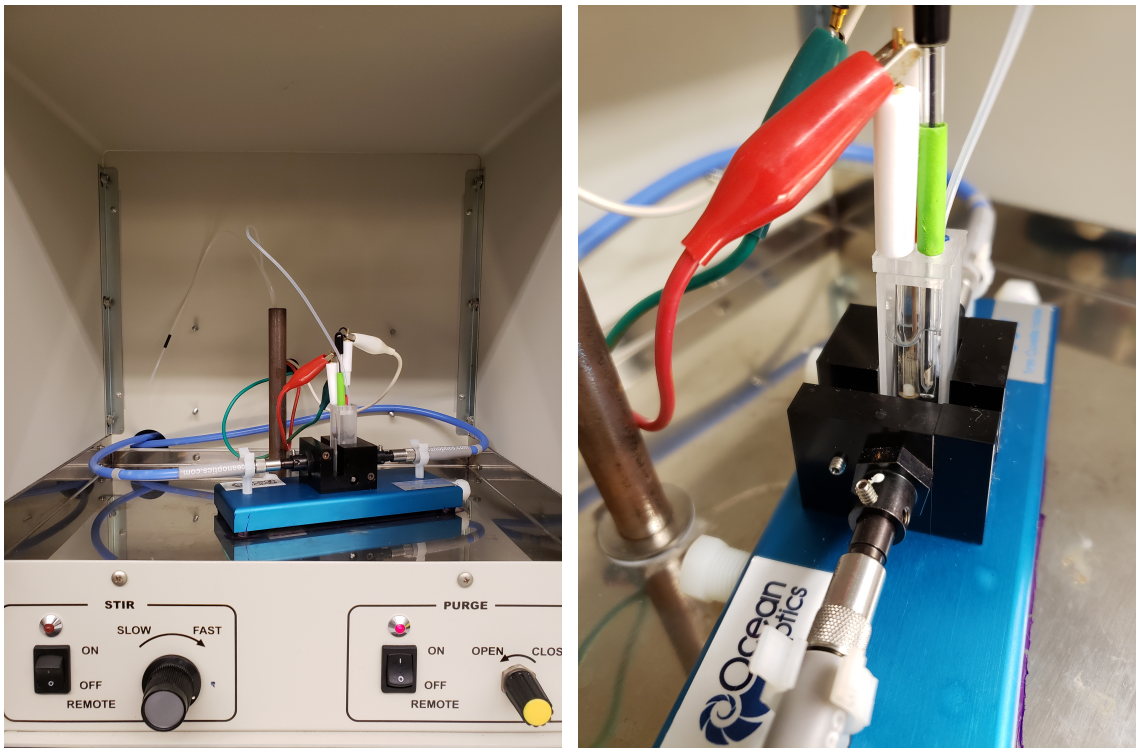

Figure A1. Photographs of the PIV/UV-vis instrumental setup. The Ocean Optics UV-vis cuvette holder is housed inside of the electrochemical cell stand.

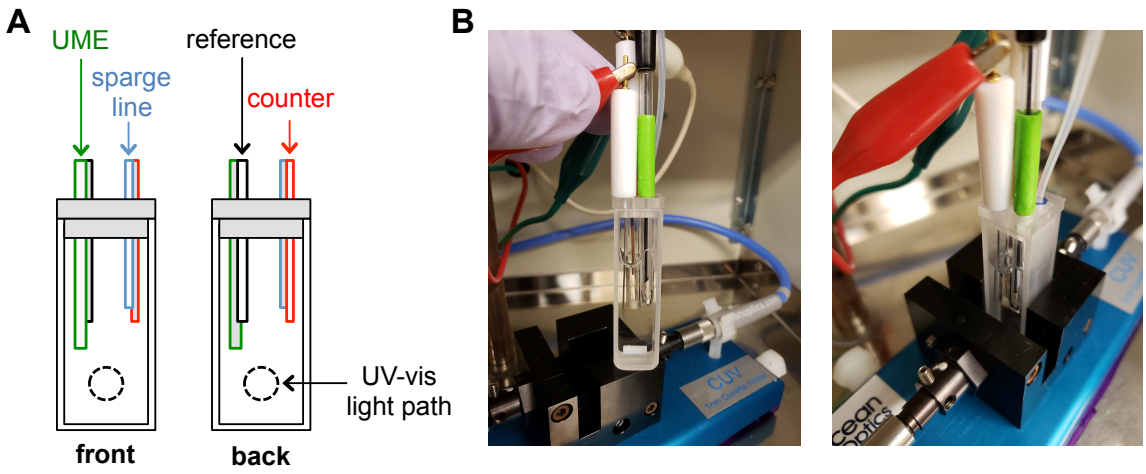

Figure A2. (A) Schematic of the front and back of the PIV/UV-vis cuvette. **(B)** Photographs of the constructed PIV/UV-vis cuvette.

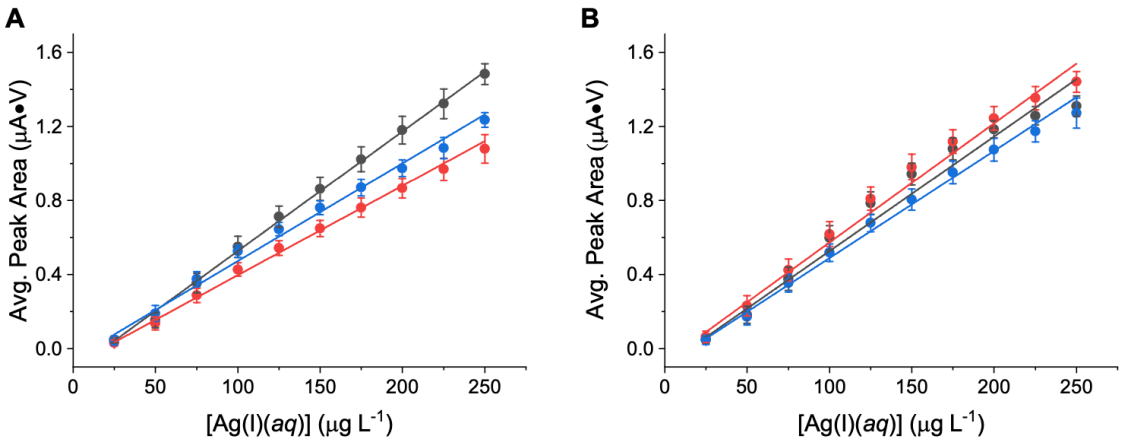

Figure A3. Triplicate calibration curves of varying concentration of Ag(I) standard in the presence of **(A)** 0 nM BSA (LOD = 7.3 μg L^{-1}) or **(B)** 2 nM BSA (LOD = 4.2 μg L^{-1}). Each calibration point represents the average and standard deviation of five consecutive stripping voltammograms. All samples were prepared in 5 mM citrate – 5 mM NaCl buffer at pH 6.5.

Table A1. BSA-Dependent AgNP Dissolution Rate Constants, $k_{dissolution}$

Nominal AgNP Diameter (nm)	$k_{dissolution}$ ($\times 10^{-3}$ min^{-1})[a]			
	0 nM BSA	0.5 nM BSA	1 nM BSA	2 nM BSA
10	0.77 ± 0.12	0.95 ± 0.25	1.4 ± 0.4	2.0 ± 0.7
20	0.22 ± 0.05	0.38 ± 0.14	0.46 ± 0.11	0.53 ± 0.07
40	0.19 ± 0.07	0.21 ± 0.04	0.27 ± 0.13	0.33 ± 0.06

[a]Experimental conditions were reported as in **Figure 3**. Each rate constant represents the average and standard deviation of three replicate LSSV experiments.

Table A2. Characterization of AgNPs in the presence and absence of BSA[a]

Nominal AgNP Diameter (nm)	[BSA] (nM)	d_{DLS} (nm)	ζ (mV)
10	0	15.4 ± 0.2	-28±2
	8	16.0 ± 0.1	-26±2
20	0	25.4 ± 0.3	-38±1
	8	25.4 ± 0.2	-38±1
40	0	42.1 ± 0.2	-39±1
	8	44.1 ± 0.5	-34±1

[a]All samples were prepared to a total silver concentration of 4.0 mg L^{-1} in citrate buffer.

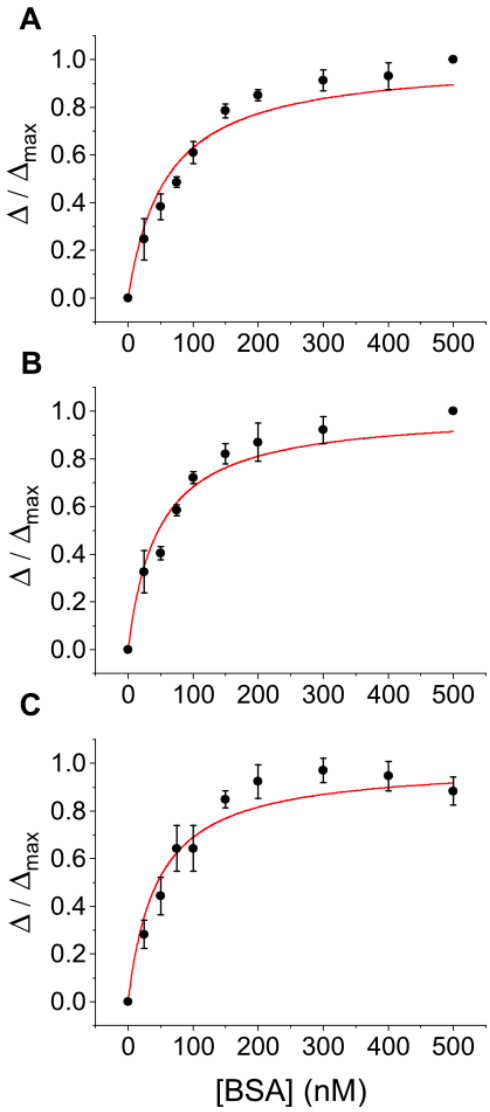

Figure A4. Langmuir adsorption isotherms of **(A)** 10 nm AgNPs, **(B)** 20 nm AgNPs, and **(C)** 40 nm AgNPs with various concentrations of BSA ranging from 0 to 500 nM. AgNPs were prepared to the same total Ag concentration = 4.0 mg L^{-1} (molar particle concentrations were as follows: 10 nm AgNPs ≈ 1.2 nM, 20 nm AgNPs ≈ 0.2 nM, and 40 nm AgNPs ≈ 0.02 nM). All samples were prepared in 5 mM citrate buffer at pH 6.5 and the isotherms were recorded using UV− vis spectroscopy.

Table A3. Association Constants, K_a, of BSA with AgNPs of Varying Diameters[a]

d_{AgNP} (nm)	K_a ($\times 10^7$ M^{-1})	R^2
10	1.7 ± 0.2	0.96
20	2.1 ± 0.3	0.96
40	2.2 ± 0.3	0.97

[a]Experimental conditions are as reported in **Figure A4**.

Table A4. Effect of AgNP diameter on the % α-helicity of BSA

Sample[a]	% α-helicity[b]
BSA Only	57.2 ± 1
10 nm AgNPs	53.8 ± 2
20 nm AgNPs	56.4 ± 1
40 nm AgNPs	50.1 ± 2

[a]Experimental conditions were as reported in **Figure 5**.
[b]Percent α-helicity was calculated using Eqns. 6 & 7.

Table A5. Dissolution Rate Constants, $k_{dissolution}$, of AgNPs in SSW[a]

[NaCl] (%w/v)	**pH**	$\boldsymbol{k_{dissolution}}$ **($\times 10^{-4}$ min^{-1})**
0.05	4.5	6.1 ± 0.7
0.05	5.0	5.1 ± 0.7
0.05	5.5	2.8 ± 0.3
0.25	5.0	16.8 ± 0.5
0.50	5.0	25.4 ± 0.1

[a]Experimental conditions were as reported in **Figures 6 and 7**.

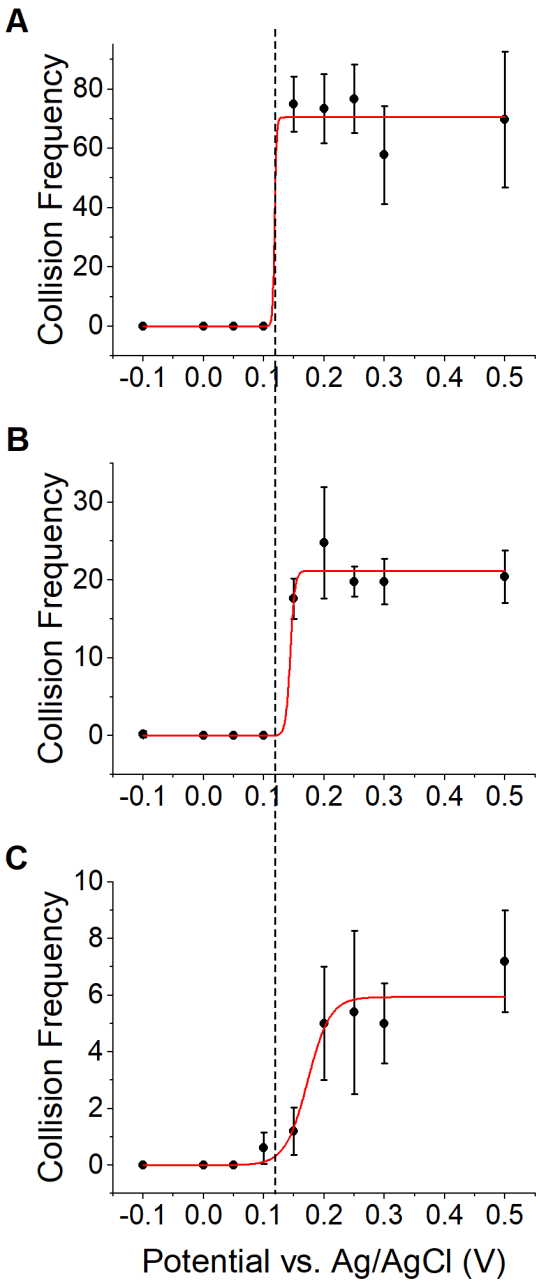

Figure A5. Plots of the AgNP collision frequency (number of collisions per 60 s) as a function of the applied potential for AgNP diameters of **(A)** 20 nm, **(B)** 40 nm, and **(C)** 80 nm. The dashed line indicates the onset potential of current transients for 20 nm AgNPs. A marked anodic shift of the onset potential is observed with increasing AgNP diameter. Error bars represent the standard deviation of 5 independent measurements. AgNPs were prepared to a final concentration of 2.0 mg L^{-1} in 10 mM citrate – 10 mM NaCl buffer (pH 5.0).

Table A6. Effect of [NaCl] on PIV collision frequencies and UV-vis aggregation rate constants, $k_{aggregation}$, determined by PIV/UV-vis[a]

[NaCl] (mM)	PIV Collision Frequency[b]	$k_{aggregation}$ ($\times 10^7$ s^{-1} M^{-1})[c]	Average R^2 (from UV-vis analysis)
10	90 ± 20	0.3 ± 0.2	0.847
20	60 ± 20	3 ± 2	0.919
40	22 ± 10	11 ± 1	0.959
60	16 ± 4	12 ± 1	0.923
80	11 ± 7	12 ± 1	0.900
100	14 ± 10	12 ± 1	0.914

[a] All AgNPs were diluted to a concentration of 5.0 mg L^{-1} in 10 mM sodium citrate (pH 5.0) with the indicated concentration of NaCl

[b]PIV collision frequencies are the number of current transients observed over 5 min and represent the average and standard deviation of 5 replicates

[c]Aggregation rate constants, $k_{aggregation}$, were calculated from UV-vis analysis using Eqn. 1 and represent the average and standard deviation of 5 replicates

Table A7. Effect of [$MgCl_2$] on PIV collision frequencies and UV-vis aggregation rate constants, $k_{aggregation}$, determined by PIV/UV-vis[a]

[$MgCl_2$] (mM)	PIV Collision Frequency[b]	$k_{aggregation}$ ($\times 10^7$ s^{-1} M^{-1})[c]	Average R^2 (from UV-vis analysis)
1.0	70 ± 20	0.17 ± 0.04	0.579
2.0	42 ± 8	5 ± 3	0.965
2.5	29 ± 4	8 ± 1	0.988
3.0	10 ± 2	12 ± 1	0.968
4.0	9 ± 2	11 ± 1	0.954
5.0	10 ± 5	12 ± 1	0.950

[a]All AgNPs were diluted to a concentration of 5.0 mg L^{-1} in 10 mM sodium citrate (pH 5.0) with the indicated concentration of $MgCl_2$

[b]PIV collision frequencies are the number of current transients observed over 5 min and represent the average and standard deviation of 5 replicates

[c]Aggregation rate constants, $k_{aggregation}$, were calculated from UV-vis analysis using Eqn. 1 and represent the average and standard deviation of 5 replicates

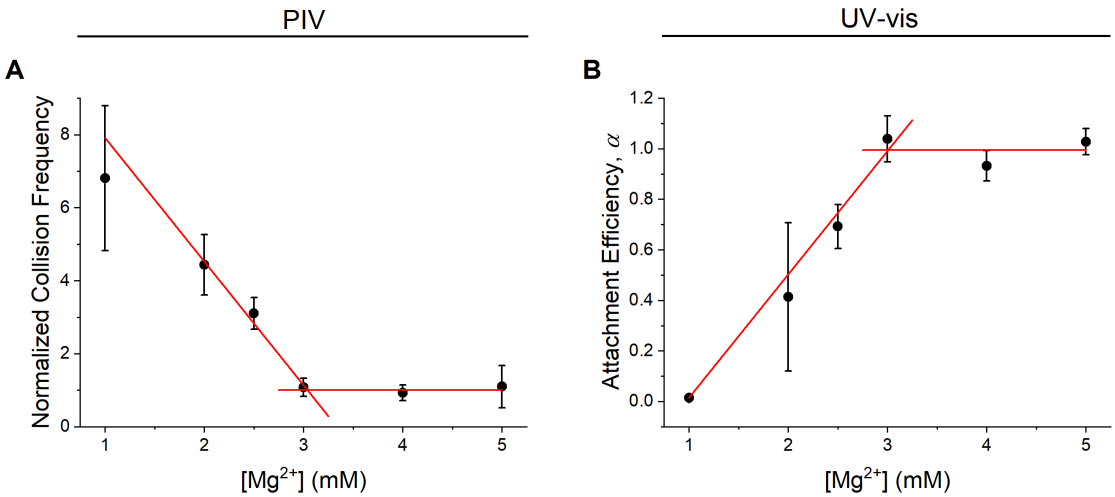

Figure A6. Determination of CCC values of AgNPs in $MgCl_2$ using PIV/UV-vis. **(A)** Normalized collision frequencies and **(B)** UV-vis attachment efficiencies are plotted as a function of the cation concentration and the intersection of the RLCA and DLCA regimes (linear curves at low and high cation concentration, respectively) is used to determine the CCC.

Table A8. Characterization of AgNPs in NaCl solutions[a]

[NaCl] (mM)	d_{PIV} (nm)	d_{DLS} (nm)	PDI	ζ (mV)
10	41 ± 8	46 ± 2	0.23 ± 0.01	-41 ± 1
20	37 ± 7	50 ± 3	0.43 ± 0.01	-43 ± 1
40	40 ± 10	190 ± 60	0.60 ± 0.01	-48 ± 2
60	39 ± 7	320 ± 20	0.24 ± 0.01	-53 ± 3
80	38 ± 8	340 ± 20	0.24 ± 0.03	-50 ± 2
100	38 ± 7	400 ± 40	0.24 ± 0.02	-54 ± 2

[a]All AgNPs were diluted to a concentration of 5.0 mg L^{-1} in 10 mM sodium citrate (pH 5.0) with the indicated concentration of NaCl. For PIV analysis, samples were analyzed immediately after introduction of NaCl. For DLS and zeta potential experiments, samples were incubated for 10 min prior to analysis. All values are reported as the average and standard deviation of 5 replicates.

Table A9. Characterization of AgNPs in $MgCl_2$ solutions[a]

[$MgCl_2$] (mM)	d_{PIV} (nm)	d_{DLS} (nm)	PDI	ζ (mV)
1.0	30 ± 20	48 ± 5	0.7 ± 0.2	-42 ± 2
2.0	40 ± 10	360 ± 20	0.44 ± 0.08	-38 ± 1
2.5	60 ± 20	460 ± 30	0.3 ± 0.4	-39 ± 1
3.0	40 ± 10	360 ± 30	0.33 ± 0.02	-36 ± 1
.0	60 ± 50	340 ± 30	0.31 ± 0.03	-33 ± 1
5.0	50 ± 10	490 ± 10	0.26 ± 0.03	-28 ± 1

[a]All AgNPs were diluted to a concentration of 5.0 mg L^{-1} in 10 mM sodium citrate (pH 5.0) with the indicated concentration of $MgCl_2$. For PIV analysis, samples were analyzed immediately after introduction of $MgCl_2$. For DLS and zeta potential experiments, samples were incubated for 10 min prior to analysis. All values are reported as the average and standard deviation of 5 replicates.

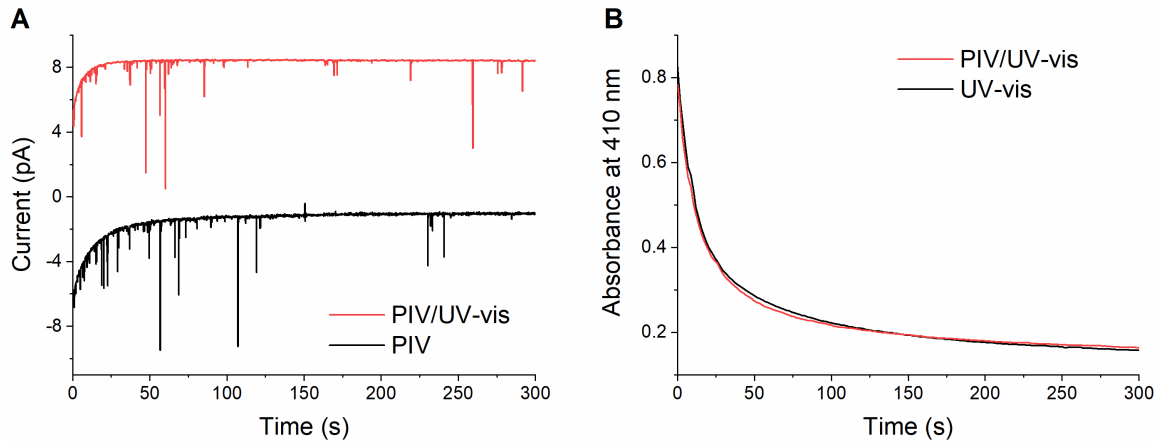

Figure A7. Control experiments demonstrating independent and integrated PIV and UV-vis analyses. **(A)** Representative amperometric *i-t* curves for PIV alone or combined with UV-vis and **(B)** representative kinetic absorbance scans for UV-vis alone or combined with PIV. AgNPs were prepared to a final concentration of 5.0 mg L^{-1} in 10 mM citrate – 40 mM NaCl buffer (pH 5.0).

Table A10. PIV collision frequencies and UV-vis aggregation rate constants, $k_{aggregation}$, for independent and combined PIV/UV-vis analysis[a]

Experiment	PIV Collision Frequency[b]	$k_{aggregation}$ ($\cdot 10^7$ $s^{-1}M^{-1}$)[c]
PIV/UV-vis	22.4 ± 10	11.1 ± 1
PIV	25.4 ± 10	-
UV-vis	-	11.8 ± 0.1

[a]All AgNPs were diluted to a concentration of 5 mg L^{-1} in 10 mM sodium citrate - 40 mM NaCl at pH 5.0
[b]PIV collision frequencies are the number of current transients observed over 5 min and represent the average and standard deviation of 5 replicates
[c]Aggregation rate constants, k aggregation, were calculated from UV-vis analysis using the slope of the linear fit and represent the average and standard deviation of 5 replicates

Figure A8. Low load (left) and high load (right) cotton fabrics synthesized by Justin Gorham (NIST). XPS analysis was used to determine the Ag loading: 0.16% for the low load fabric and 0.31% for the high load fabric.

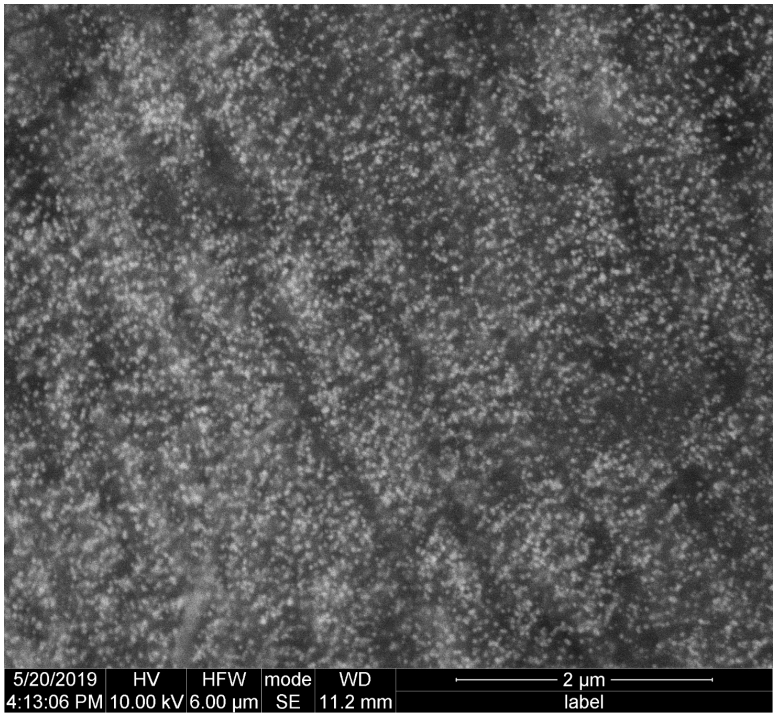

Figure A9. Representative SEM image of the high load cotton fabric showing the presence of AgNPs (white spheres). A crude estimate of the AgNP diameter was obtained using 41 particles and determined to be 63 ± 13 nm.